

UNCLASSIFIED

AD-464807 |

DEFENSE DOCUMENTATION CENTER

FOR

SCIENTIFIC AND TECHNICAL INFORMATION

CAMERON STATION ALEXANDRIA, VIRGINIA



UNCLASSIFIED

NOTICE: When government or other drawings, specifications or other data are used for any purpose other than in connection with a definitely related government procurement operation, the U. S. Government thereby incurs no responsibility, nor any obligation whatsoever; and the fact that the Government may have formulated, furnished, or in any way supplied the said drawings, specifications, or other data is not to be regarded by implication or otherwise as in any manner licensing the holder or any other person or corporation, or conveying any rights or permission to manufacture, use or sell any patented invention that may in any way be related thereto.

2
0
0
4
6
1
CATALOGED BY:
AC 175
AC 175

Technical Report 26

THE USE OF ION PROBES IN RE-ENTRY PHYSICS

By: H. R. BREDFELDT W. E. SCHARFMAN H. GUTHART T. MORITA

Prepared for:

ADVANCED RESEARCH PROJECTS AGENCY
THE PENTAGON
WASHINGTON, D.C. 20301
ATTN: CLIFFORD E. McLAIN

CONTRACT SD-103 UNDER
ARPA ORDER 281-62
PROJECT CODE 7400

STANFORD RESEARCH INSTITUTE

MENLO PARK, CALIFORNIA

*SRI

4 6 4 8 0 7

DDC AVAILABILITY NOTICE

**QUALIFIED REQUESTERS MAY OBTAIN COPIES
OF THIS REPORT FROM DDC.**



May 1965

Technical Report 26

THE USE OF ION PROBES IN RE-ENTRY PHYSICS

Prepared for:

ADVANCED RESEARCH PROJECTS AGENCY
THE PENTAGON
WASHINGTON, D.C. 20301
ATTN: CLIFFORD E. McLAIN

CONTRACT SD-103 UNDER
ARPA ORDER 281-62

By: H. R. BREDFELDT W. E. SCHARFMAN H. GUTHART T. MORITA
ELECTROMAGNETIC SCIENCES LABORATORY

SRI Project 3857

Approved: D. R. SCHEUCH, EXECUTIVE DIRECTOR
ELECTRONICS AND RADIO SCIENCES

61
Copy No.

ABSTRACT

Classical (Langmuir) probe theory is reviewed and the conditions under which it is applicable to the re-entry physics problem identified. Some later developments in probe theory, which account for flow velocity in the free-molecular case, are presented.

Measurements of current densities have been made with ion probes mounted flush in the walls of a pressure-driven shock tube; the results are interpreted using a one-dimensional, collision-dominated probe theory, allowing for the spatial nonuniformities in ion density. Correlation of the probe theory with a zero-order gas dynamic boundary layer theory is shown to lead to theoretical current estimates in fair agreement with the experimentally observed values.

Some shock ionization precursor results in air are also presented. Finally, the results of some calibrations on probes that were flown on the RVIP and LORV programs are presented.

CONTENTS

ABSTRACT	ii
LIST OF ILLUSTRATIONS	iv
I INTRODUCTION	1
II ELECTROSTATIC PROBE THEORY	3
A. Operation of Probes—Classical Theory	3
B. Conditions for Applicability of Classical Probe Theory	7
C. Ion Collection with Flow Velocity—Free-Molecular Case	8
D. Ion Collection by Flush Probes in Nonuniform Plasmas	11
III FLUSH ION PROBE EXPERIMENTS	14
A. Test Conditions	14
B. Flush Probe Measurements	15
C. Results	20
D. Correlation with Theory	23
E. Summary and Conclusions	28
F. Future Work	29
IV PRECURSOR MEASUREMENTS	33
V RVIP FLIGHT TEST CALIBRATIONS	36
A. Measurements	36
1. General Electric Probe	36
2. AVCO Flush-Mounted Langmuir Probe	40
B. Conclusions and Recommendations	41
APPENDIX A GAS-DYNAMIC BOUNDARY LAYER THEORY	43
APPENDIX B PRESSURE-DRIVEN SHOCK TUBE	55
APPENDIX C TEST FACILITIES USED IN THE RVIP EXPERIMENTAL PROGRAM	70
REFERENCES	76

ILLUSTRATIONS

Fig. 1	Ratio of Directed to Random Velocity as a Function of the Normalized Current Collected by a Probe Perpendicular to the Directed Velocity	9
Fig. 2	Nondimensional Flux Density of Attracted Particles as a Function of Dimensionless Probe Potential for Various Speed Ratios, S , at $a/r_p = 100$	10
Fig. 3	Configuration of Flush Ion Probes	15
Fig. 4	Ion Probe Circuitry	17
Fig. 5	Time-Resolved Response of HB-2 Ion Probe	17
Fig. 6	Typical Time-Resolved Response of HB-1 Ion Probe for Intermediate and High Free-Stream Ion Densities	18
Fig. 7	Typical Time-Resolved Response of HB-1 Ion Probe for Low Free-Stream Ion Densities	19
Fig. 8	Response of HB-1 Ion Probe to Turbulent Free-Stream Conditions	20
Fig. 9	Experimental and Theoretical Flush Ion Probe Current Densities Vs. Free-Stream Equilibrium Ion Density	21
Fig. 10	Normalized Temperature and Mass Density Profiles through the Laminar Boundary Layer on a Flat Plate	25
Fig. 11	Normalized Velocity Profile and Normalized Ion Density Profile through the Laminar Boundary Layer on a Flat Plate	26
Fig. 12	Experimentally Determined Collision-Dominated Sheath Thickness for the Flush Ion Probe Vs. Free-Stream Ion Density	28
Fig. 13	Experimental Arrangement of Cylindrical Ion Probes and Flush Probes on a Flat Plate to Measure Ion Density Profile through the Boundary Layer . . .	30
Fig. 14	Characteristic Ion Probe Responses	31
Fig. 15	Reduced Experimental Data for Fig. 14 Superimposed on Normalized Theoretical Boundary Layer Ion Density Profile	32
Fig. 16	Time-Resolved Microwave Interferometer and Ion Probe Responses from Ionization Precursor Measurements	33
Fig. 17	Measured Precursor Ionization Profiles in Air Ahead of the Shock Front . . .	34
Fig. 18	RVIP Probe Geometries Used in Calibration	37
Fig. 19	Ion Density as a Function of Ion Saturation Current for the General Electric Probe	38
Fig. 20	Ion Density Inferred from General Electric Probe Vs. Density Measured with Standard Probe	39
Fig. 21	Langmuir Characteristic of General Electric Probe in the Flame Facility . . .	40
Fig. 22	Sperry Flush-Mounted Probe	42
Fig. B-1	Schematic Layout of Pressure-Driven, Arc-Heated Shock Tube	57
Fig. B-2	Cross Section of Shock Tube Driver	58
Fig. B-3	Shock Velocity Measurement on Raster Scope	59

ILLUSTRATIONS

Fig. B-4	Comparison of Flush-Mounted Pressure Probe Response and 0.25 x 6.3 mm Free-Stream Ion Probe Response	59
Fig. B-5	Typical Photomultiplier Response for 1 mmHg Initial Shock Tube Pressure	60
Fig. B-6	Typical Photomultiplier Response for 0.1 mmHg Initial Shock Tube Pressure and Low Shock Velocity at that Pressure	61
Fig. B-7	Image Converter Pictures	62
Fig. B-8	Shock Velocity Vs. Capacitor Voltage for Pressure-Driven, Arc-Heated Shock Tube	63
Fig. B-9	Shock Tube Test Times Vs. Shock Velocity at 1 mmHg Initial Shock Tube Pressure	64
Fig. B-10	Shock Tube Test Times Vs. Shock Velocity at 0.1 mmHg Initial Shock Tube Pressure	65
Fig. B-11	Experimental Configuration of Microwave Interferometer	67
Fig. B-12	Equilibrium Slug Electron Density Measured with Microwave Interferometer at 0.1 mmHg Initial Shock Tube Pressure and Response of 0.25 mm dia Free-Stream Ion Probe	68
Fig. B-13	Equilibrium Slug Electron Density Measured with Microwave Interferometer at 1 mmHg Initial Shock Tube Pressure and Response of 0.25 mm dia Free-Stream Ion Probe	68
Fig. C-1	Detail of Conical Discharge Section of the Electromagnetic Shock Tube	72
Fig. C-2	Photograph of Electromagnetic Shock Tube	73
Fig. C-3	Ethylene-Oxygen Flame Burning at 8 mmHg Pressure	75

I INTRODUCTION

The determination of the electron density surrounding a re-entry vehicle from gas-dynamic calculations is hampered by uncertainties in the rate constants of the ionization and de-ionization processes as well as by the effects of ablation products. However, calculations have been made for ionization in air (i.e., with no ablation products); and it would be desirable to be able to compare these calculations against flight-test data.

One common method of determining electron density is to measure the absorption and phase shift of microwaves that propagate through the plasma. However, these measurements give only limited information; only integrated values for absorption and phase shift can be obtained. In order to interpret the results in terms of electron density and collision frequency, it is necessary to estimate the spatial distributions of these parameters, although the spatial distribution is itself one of the parameters that one would like to obtain from measurements. In addition, the dynamic range of parameters that can be measured by such methods in a realistic flight test is usually small. For a given microwave frequency, it is usually possible to determine the electron density only when the plasma frequency is of the order of the microwave frequency.

An alternative technique for measuring electron density during flight tests is to use an electrostatic probe. These probes can be designed so that measurements can be made with a spatial resolution of less than 1 mm. Thus, the use of a probe that could move radially outward from the re-entry vehicle would make it possible to determine the spatial distribution of electrons. (One could also use several probes mounted at different radial distances from the surface.) Electrostatic probes are inherently capable of measuring a wide range of electron densities, since their use involves only the measurements of voltages and currents that change relatively slowly.

Classical probe theory, as developed by Langmuir, is predicated upon a number of conditions that will not hold true over an entire trajectory.^{1*}

* References are listed at the end of the report.

It is necessary to determine the errors involved in the inferred plasma parameters and to develop a theory that will enable interpretation of the data over the complete trajectory.

In this report, the classical Langmuir probe theory has been reviewed and the conditions under which it is applicable pointed out. Recent developments in probe theory that account for flow velocity in the free-molecular case are subsequently presented in this report.

Preliminary measurements have been made with flush ion probes mounted in the walls of a pressure-driven shock tube. In this position, the flush probes are exposed to the large ion-density, temperature, and velocity gradients existing in the boundary layer in the vicinity of the cold wall. The measured current densities are interpreted using a one-dimensional, collision-dominated, probe theory, allowing for the spatial nonuniformities in ion density. Correlation of the probe theory with a zero-order gas dynamic boundary layer theory has led to theoretical current estimates in fair agreement with the experimentally observed values.

Some shock ionization precursor results in air are also presented. Finally, the results of some calibrations on probes that were flown on the Re-entry Vehicle Instrumentation Program (RVIP) and Low Observable Re-entry Vehicle (LORV) programs are given. As a result of these and many other measurements using probes, it is concluded that measurements in the saturated-ion-current side of the Langmuir characteristic are considerably more accurate than measurements on the electron-current side near plasma potential.

II ELECTROSTATIC PROBE THEORY

A. OPERATION OF PROBES--CLASSICAL THEORY

An electrode or probe inserted into a plasma will collect charges until it has sufficiently high potential with respect to the plasma to neutralize the net charge arriving at the electrode, *i.e.*, the electrode potential is such as to equalize the electron and ion flux. If the electrode potential is made increasingly negative with respect to a second electrode, fewer and fewer electrons will reach the probe until only positive ions are collected. Conversely, if the probe potential is made increasingly positive with respect to the second electrode (and the area of the second electrode is greater than that of the first by the square root of the mass ratio of ions to electrons), the probe will collect only electrons.

When electrostatic probes are used to collect electrons, the saturated electron current density, J_- , is related to the electron density, n_- , by the expression

$$J_- = \frac{n_- e v_-}{4}$$

where

$$v_- \text{ is the electron random velocity} = \sqrt{\frac{8kT_-}{\pi m_-}}$$

e is the electron charge

k is Boltzmann's constant

T_- is the electron temperature

m_- is the electron mass.

When ions are collected, the relationship between ion current density and ion density (or electron density, assuming that $n_- = n_+$) has been shown by Bohm *et al.*² to be approximately

$$J_+ = 0.4n_+ e v_+ , \quad (1)$$

where

$$v_+ \text{ is the velocity with which ions reach the sheath} = \left(\frac{2kT_-}{m_+} \right)^{\frac{1}{2}}$$

m_+ is the ion mass.

From the expression for saturated ion current density, it can be seen that, if the ion mass and electron temperature are known or can be estimated, a measurement of the ion current density is sufficient to determine the electron density. Estimates can often be made of ion species, and hence ion mass; in addition, the electron temperature also may be estimated from gas-dynamic considerations. In either case, errors in these quantities will not be very serious, since they both enter into the expression for current density as the square root. For example, if the temperature at a certain region on a re-entry vehicle is estimated at 3000°K when it is really only 2500°K, the error in ion density is only about 10 percent.

Between these two saturated regions is a region that may be used to determine the electron temperature.

For potentials below plasma potential, the electrons see a potential barrier that only the higher energy electrons can overcome to be collected at the electrode. If, at the sheath edge, the random electron current density is J_- , then at a point in the sheath where the potential is V volts below the plasma potential, the electron current density is $J_- \exp(-eV/kT_-)$.

The net current density is the algebraic sum of the ion and electron current densities, so that the net current density is

$$J_{\text{net}} = J_- \exp(-eV/kT_-) - J_+ . \quad (2)$$

Bringing the ion current density to the left side of the equation and taking logarithms of both sides, we obtain

$$\ln(J_+ + J_{\text{net}}) = \ln J_- - eV/kT_- . \quad (3)$$

Thus T_- may be found from a semilogarithmic plot of $J_+ + J_{\text{net}}$ as a function of V . This plot will be a straight line with slope e/kT_- for a Maxwellian energy distribution.

Since we have found that measurements on the ion-saturation-current side are more accurate than measurements on the electron-saturation-current side, we shall restrict the following discussion to the ion side.

In making probe measurements, one measures current, rather than current density. Therefore, it is necessary to know the relation between these two quantities. From a consideration of the formation of plasma sheaths, the sheath thickness, d_s , can be approximated by

$$d_s \approx \lambda_D \eta^{3/4} \quad (4)$$

where

$$\lambda_D = \text{Debye length} = \sqrt{\frac{\epsilon_0 k T_e}{N_e e^2}} \approx 7 \sqrt{\frac{T_e}{N_e}} \text{ cm}$$

$$\eta = \left| \frac{eV}{kT_e} \right|$$

and ϵ_0 is the permittivity of free space. Equation (4) is the expression for the sheath thickness for space-charge-limited flow in a planar geometry. This equation is obtained by equating the current density given by the planar space charge equation to the random current density of Eq. (1). The approximation of a planar solution for sheath thickness is applicable to nonplanar probes only when the sheath thickness is small compared to the probe radius. When the sheath thickness is large, it can be shown¹ that the current collected by a probe may be made independent of the sheath dimensions, so that the approximation of Eq. (4) is no longer required.

The overall sheath radius, a , is given by

$$a = r_p + d_s, \quad (5)$$

where r_p is the probe radius. If the probe radius is larger than the sheath thickness, then all the particles that pass through the sheath edge will be collected by the probe and the probe area will be approximately equal to the sheath area. Under these conditions, the probe current for a cylindrical probe is

$$I_+ = 2\pi r_p L J_+ \quad (6)$$

and for a spherical probe

$$I_+ = 4\pi r_p^2 J_+ , \quad (7)$$

where

I_+ is the probe current

L is the probe length.

A further consequence of requiring the probe sheath to be of the same order as the probe radius is that the probe current will be relatively insensitive to the probe potential, so long as the potential is sufficiently negative to draw saturation current. This is so because the increase in probe current with potential is due to an increase in the sheath thickness, which increases the area through which current passes. However, since the sheath area is approximately equal to the probe area, there will be no significant change in the current-collecting area.

In order to ensure this condition, it is necessary that

$$r_p \gg d_s$$

and that the probe potential be such that

$$\eta = \left| \frac{eV}{kT_e} \right| \gg 1 .$$

If these conditions are not satisfied, the current will be a function of voltage and will no longer be simply equal to the product of the random current density and the physical area. Interpretation of probe current in terms of electron densities under these conditions becomes more complicated, but verified theories for such interpretations are available.³⁻⁵ The results are summarized in the following.

When $\eta \gg a/r_p$, where a is the sheath radius and r_p is the probe radius, the current is independent of potential but is a function of a/r_p :

$$I_+ = (a/r_p) 2\pi r_p L J_+ \text{ (for a cylindrical probe)}$$

and

$$I_+ = (a/r_p)^2 4\pi r_p^2 J_+ \text{ (for a spherical probe).}$$

When $\eta \ll a/r_p$ and $\eta > 2$, the current is a function of potential but independent of a/r_p .

$$I_+ = 2/\pi \sqrt{\eta + 1} 2\pi r_p L J_+ \text{ (for a cylindrical probe)}$$

and

$$I_+ = \eta 4\pi r_p J_+ \text{ (for a spherical probe).}$$

These are asymptotic cases. *Hok*⁴ has calculated the dependence of ion current on ion density and temperature for a cylindrical probe for the whole range of η and (a/r_p) . For the spherical probe, the intermediate range of η and a/r_p can be approximated using the solution of *Allen, et al.*⁵

B. CONDITIONS FOR APPLICABILITY OF CLASSICAL PROBE THEORY

There are a number of conditions that must obtain for classical probe theory to be applicable.

- (1) The mean free path must be much larger than the probe dimension. This is necessary to ensure that the probe does not disturb the plasma, and may be written as

$$r_p < \lambda \text{ } (\lambda = \text{mean free path}) \text{ } .$$

- (2) The sheath thickness must be much less than a mean free path. This ensures that there are no collisions in the sheath, an assumption used in deriving the relations between current and probe potential. This may be written as

$$d_s = a - r_p < \lambda \text{ } .$$

- (3) There is no net flow velocity; this may be written as

$$v_f = 0 \text{ } .$$

- (4) There is frozen flow across the sheath; that is, there is no ionization or ionization loss—such as recombination—in the sheath. This may be expressed as a current-continuity relation

$$\nabla \cdot J = 0 \text{ } .$$

(5) The discussion so far has concentrated on the current collection properties at only one electrode. There must be another electrode in contact with the plasma to complete the circuit for current flow. This second electrode must have sufficient area for current collection that the sheath around it does not limit current flow in the system. This consideration of area is especially important in making the temperature measurement and in ensuring that conditions are proper for measuring the random electron current density. If the area is too small, a saturation current will exist for both ion and electron currents; however, the electron saturation current will be less than the full random electron current density. The area ratio is related to the ratio of mobility of electrons and ions; in air, the ratio must be at least 250.

$$\frac{\text{Area Electrode 1}}{\text{Area Electrode 2}} > 250$$

If the electrode-area ratio is less than this value, the full random electron current density will not be measured at any potential. The electron temperature can be inferred from the current/voltage plot but the interpretation will be somewhat different than that outlined above. The theory of probe operations at area ratios less than that indicated above has been worked out by Johnson and Malter.⁶

C. ION COLLECTION WITH FLOW VELOCITY—FREE-MOLECULAR CASE

Several theoretical treatments^{7,9} have investigated the case of ion collection in a flowing plasma for the case where there are no collisions in the sheath and where the probe is smaller than the mean free path. It is also usually assumed that the form of the sheath is not disturbed by the flow.

The theoretical relation between probe current and flow velocity is shown in Fig. 1 for the case where the sheath thickness is small compared to probe radius. Under these conditions, a useful parameter that indicates whether the flow has a significant effect on ion current collection is the ratio of flow velocity, v_f , to thermal velocity, v_t [$v_t = (2kT_e/m_+)^{1/2}$]. This ratio is approximately 0.8 times the Mach number for air before dissociation. When the Mach number is much less than unity, the effect of flow is negligible. When the Mach number is greater than about three, the current is essentially made up of the flow of ions into the projected area of the probe. Thus, for $a/r_p \approx 1$,

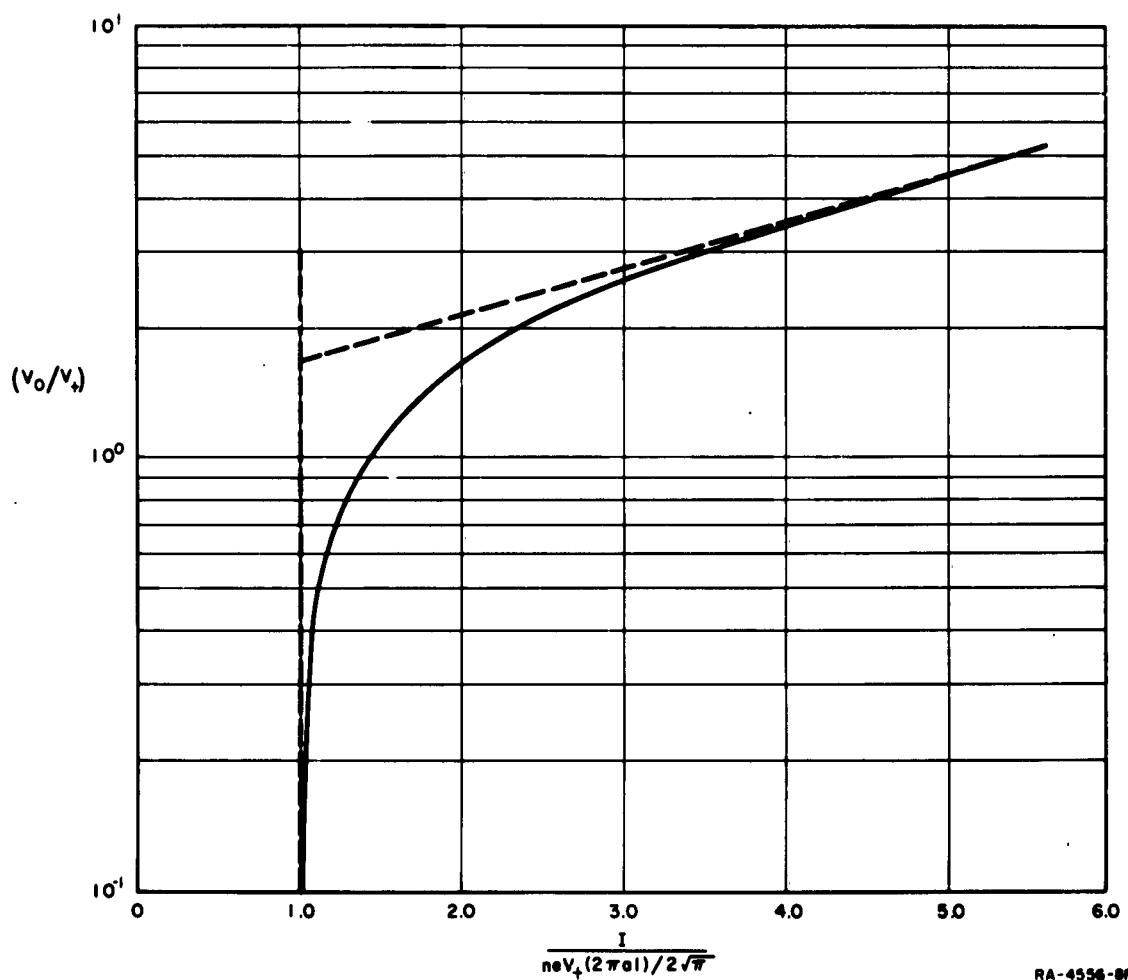


FIG. 1 RATIO OF DIRECTED TO RANDOM VELOCITY AS A FUNCTION
OF THE NORMALIZED CURRENT COLLECTED BY A PROBE
PERPENDICULAR TO THE DIRECTED VELOCITY

$$I_+ = n_+ e v_f 2 r_p L \text{ (for cylindrical probes with flow perpendicular to axis)}$$

and

$$I_+ = n_+ e v_f \pi r_p^2 \text{ (for spherical probes).}$$

When the sheath thickness is larger than the probe radius, the problem is more complicated. In addition to the Mach number, one must consider the relation between the potential field around the probe, which pulls the ions toward the probe, and the inertia of the ions, which can carry them through the potential field without being collected. This problem was treated by Smetana;⁹ his results are shown in Fig. 2. The actual current collected is obtained by multiplying the random current collected through the physical area of the probe by the factor F , given in Fig. 2.

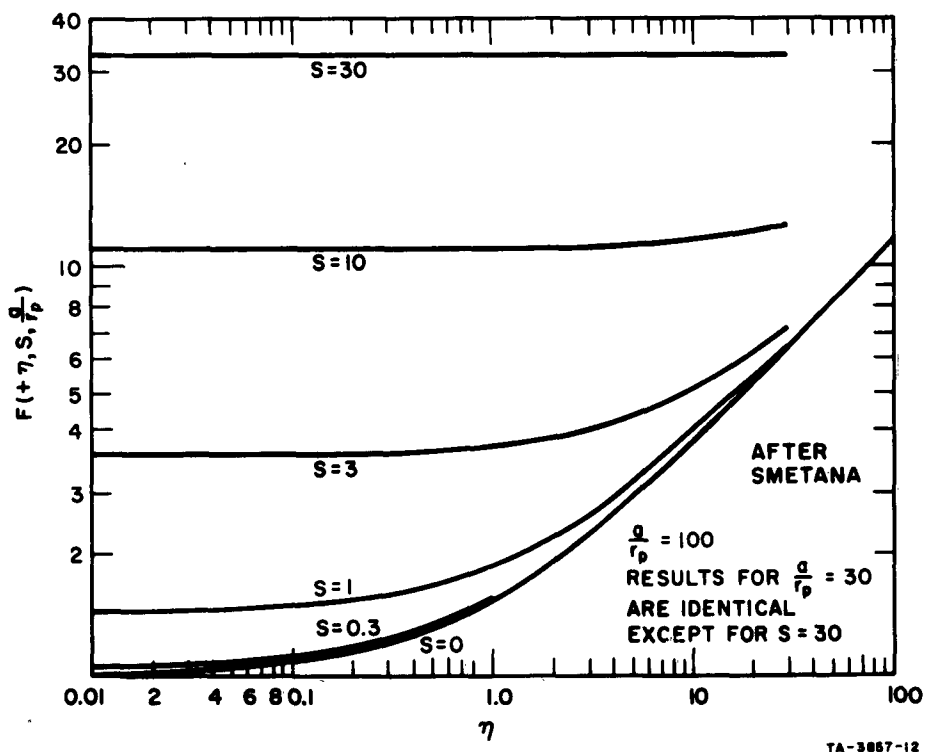


FIG. 2 NONDIMENSIONAL FLUX DENSITY OF ATTRACTED PARTICLES AS A FUNCTION OF DIMENSIONLESS PROBE POTENTIAL FOR VARIOUS SPEED RATIOS, S , AT $\frac{a}{r_p} = 100$

When S (which is v_f/v_t) is equal to zero, we have the case discussed previously when $\eta \ll a/r_p$. The current increases with $(\eta + 1)^{1/2}$. As S becomes greater than zero, the current at low values of η increases; at high values of η , the current is unchanged.

This behavior can be explained as follows. At low η and large a/r_p , the potential field is so weak that many of the ions that enter the sheath orbit past the probe and leave the sheath without being collected. Under these conditions, the current collected is equal to the random current density times the physical area of the probe. Thus, at low η , when the current is only proportional to the physical area of the probe with $S = 0$, the addition of flow increases the current collected, just as it would in the case of $a/r_p \approx 1$. At large values of S , $F \approx S$ and $I_+ \approx nev_f A_p$, where A_p is the projected area.

At higher values of η , with $S = 0$, a larger percentage of the ions that enter the sheath are collected by the probe. From simple orbital calculations one finds that, with a given potential V and for particles entering with initial energy V_0 , the radius at which particles will just be collected is $r_a = r_p(1 + V/V_0)^{1/2}$. Therefore, the current that is collected is proportional to the flux entering the sheath out to a radius r_a times the area at that radius:

$$I_+ \propto nV_0^{1/2} \times r_p(1 + V/V_0)^{1/2} .$$

For $S = 0$, $V_0 = kT_e/e$ and I_+ is given by the equation for $a/r_p > \eta$. In the limit of $\eta \gg 1$, $I_+ \propto V^{1/2} r_p$. When $S > 0$, the flux is proportional to $SV_0^{1/2}$ and $r_a = r_p(1 + V/S^2 V_0)^{1/2}$. Thus, the absorption radius is decreased while the flux entering the sheath increases so that

$$I_+ \propto nSV_0^{1/2} \times r_p(1 + V/S^2 V_0)^{1/2} .$$

When $\eta \gg S^2$, this reduces to the same value as when $S = 0$.

D. ION COLLECTION BY FLUSH PROBES IN NONUNIFORM PLASMAS

In order to avoid perturbations of the flowing plasma surrounding a re-entry vehicle, it may be necessary to place probes in the surface of the vehicle (as has been done on the LORV program), rather than into the flow field. Since the electron density varies as a function of distance

from the vehicle surface, the question arises as to what current the probe will measure.

Ordinarily, a probe samples the plasma at the edge of the sheath. For the classical case, where the mean free path is much larger than the sheath radius, the density without the probe present cannot change significantly in a sheath thickness. However, in the immediate vicinity of the vehicle surface, the electron density may be so low that the sheath extends out many mean free paths to a point where the electron density has increased significantly. Under these conditions, there will be many collisions in the sheath.

The following is a first attempt at a one-dimensional theory to handle this case.

A planar geometry is assumed with the probe sufficiently large that the physical and sheath areas are approximately equal; most of the current drifts into the sheath from a plane d_s centimeters from the surface. Assuming that there is neither recombination nor ionization in the sheath, an equation for the current may be written as:

$$I = A n_{+s} e v_{th} / 4 \quad (8)$$

where

n_{+s} = ion density at the sheath edge

v_{th} = thermal velocity at the sheath edge.

If these assumptions are correct, a measurement of the ion current coupled with a knowledge (either theoretical or from another measurement) of the thermal velocity at the sheath edge is sufficient to determine the ion density at the sheath edge. In order to establish the location of the sheath edge, it is assumed that the charge density redistributes itself within the sheath in such a manner that the current flowing across the sheath to the electrode is governed by the same relationships as for a space-charge-limited diode at high pressures.¹⁰ This relationship is given by

$$I = 9/8 \epsilon_0 \mu_+ \frac{V^2}{d_s^3} A \quad (9)$$

where

μ_+ = ion mobility

V = potential across the sheath

d_s = distance from the wall to the sheath edge

A = area of the electrode.

Equation (9) may be solved for d_s in terms of the experimental parameters, I, V and μ_+ . Equation (9) is for a constant mobility through the diode. In the case of a sheath formed near the vehicle surface, the mobility will vary through the sheath, decreasing toward the surface by a factor generally less than three. The diode equations have been solved with a mobility decreasing exponentially from the cathode. It is found that, for a decrease in mobility of a factor of three, the solution has the same form as Eq. (8) with μ_+ equal to the mobility at the sheath edge, but with the constant reduced to about three quarters of the value shown above. Considering the order of the other approximations, Eq. (8) will be used as it stands with μ_+ equal to the mobility at the sheath edge.

If these assumptions are valid, the measurement of current in an electrode flush in the vehicle surface will enable one to determine the ion flux at a distance d_s from the surface. It is interesting to note from Eq. (9) that the sheath edge may be moved by varying the probe potential, thus affording the possibility of measuring the electron density profile near the wall. The distance d_s will be a function of the plasma parameters as well as the potential. For reasonable potentials d_s will be of the order of a 0.025 mm (1 mil) for electron densities around 10^{13} electron/cc and increase to about a centimeter for densities around 10^7 electron/cc. Thus, the degree to which the boundary layer near the vehicle can be sampled by a flush probe will depend strongly upon the density levels involved.

Preliminary results using this theory to interpret data taken in a shock tube are discussed in Sec. III.

III FLUSH ION PROBE EXPERIMENTS

To date, very little experimental data is available regarding flush-mounted ion probe operation. The understanding of these probes is necessary for the evaluation of the data from the RVIP program. The only experiments known for which results have been published are those of Talbot¹¹ and Pollin,¹² which pertain to stagnation point flow conditions

The experimental determination of plasma parameters by means of ion probes mounted flush in a surface bounding the plasma necessarily restricts the spatial extent of flush probe ion collection to regions within the boundary layer. This means that, for cold surfaces, the flush ion probes operate in spatial regimes where large ion density gradients, thermal gradients, and velocity gradients exist. In addition, because of the relatively low ion concentrations in the immediate vicinity of the wall, the probe sheath may no longer be free-molecular.

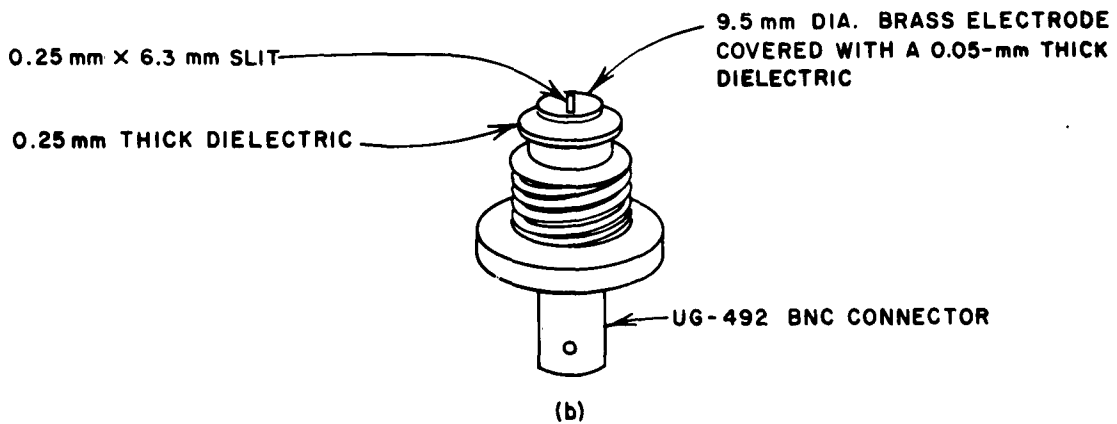
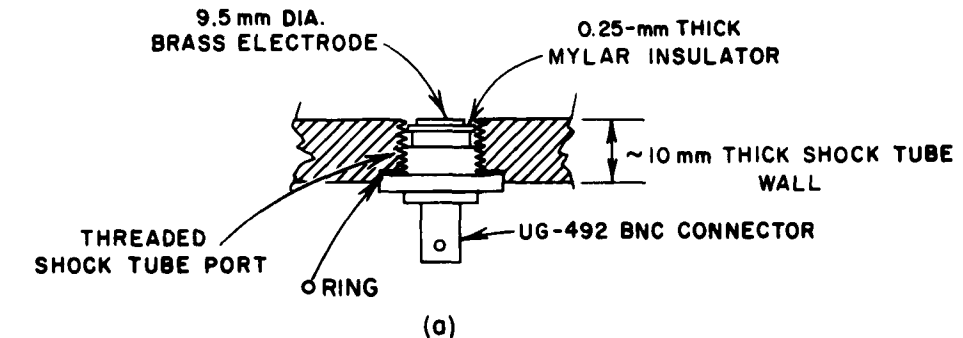
A. TEST CONDITIONS

To obtain preliminary information on flush ion probe operation in high-velocity, high-temperature, free-stream conditions, an experimental program was undertaken at SRI in the 12-inch diameter, pressure-driven shock tube. In this exploratory program, ion probes of various geometries and sizes were mounted flush in the shock tube wall. In this position the ion probes were separated from the free-stream plasma by a nonequilibrium, nonsteady, high-velocity boundary layer. No particular care was taken to remove the driver impurities from the shock tube walls nor to improve the tube wall roughness (corresponding to a standard, 12-inch diameter, schedule 40, aluminum tube). Untreated room air was used as the test gas. A detailed description of the shock tube is given in Appendix B of this report.

All experiments in this series were run at 1 mmHg initial pressure, with shock velocities ranging from 2.8 to 6 mm/ μ sec. The corresponding range of theoretical free-stream ion density varied from 10^{10} to 2×10^{14} ions/cc. The total test times measured from the arrival of the pressure discontinuity to the arrival of the interface, as monitored by photomultipliers and free-stream ion probes, varied from zero to about 100 μ sec.

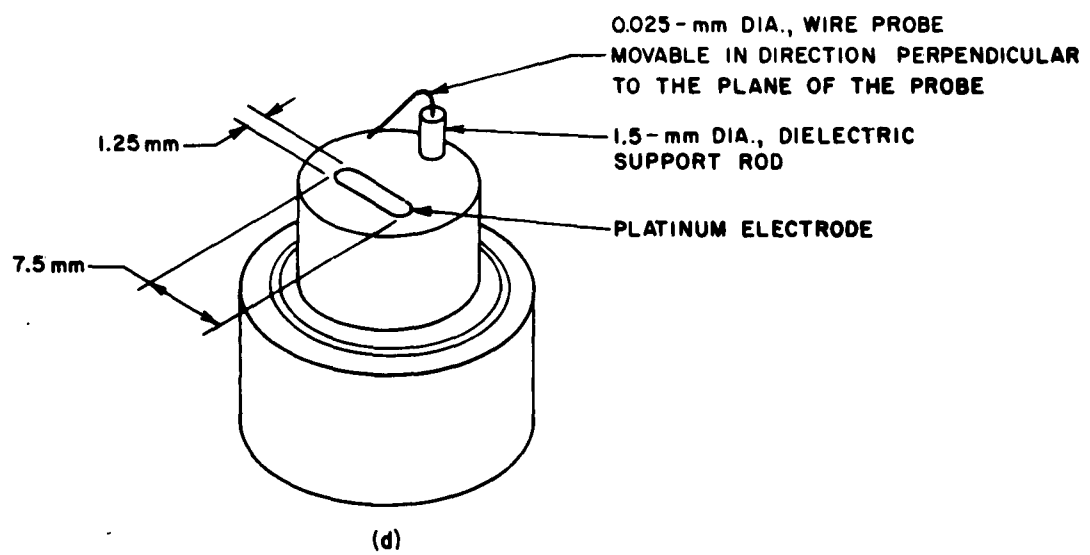
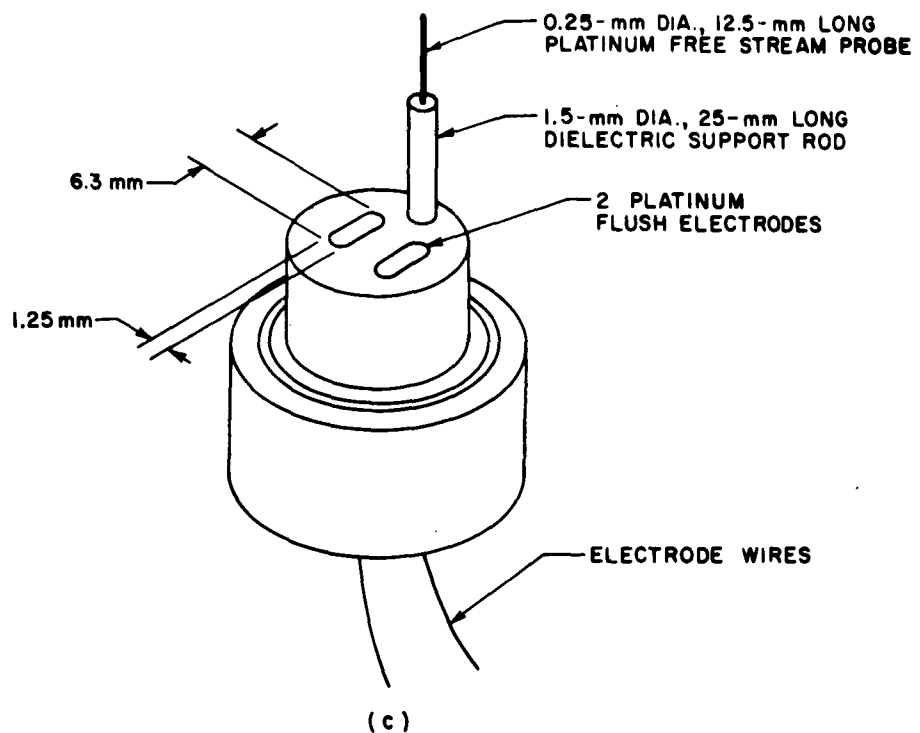
B. FLUSH PROBE MEASUREMENTS

Probe geometries and the associated probe circuitry are shown in Figs. 3 and 4. Probe geometries tested included a 9.5-mm diameter circular electrode and three strip electrodes of approximate size 6.3×1.25 mm (HB-1), 7.5×1.25 mm (HB-2) and $6.3 \text{ mm} \times 0.25 \text{ mm}$. Since all probes were connected to a common ground through the oscilloscopes, they were operated as unequal area probes; the shock tube wall served as the second, circuit-completing electrode. Free-stream electron densities were checked in a separate experimental series by microwave interferometer measurements. Over the range of free-stream conditions covered, the agreement with theoretical equilibrium values corresponding to shock velocities was better than a factor of two.



TA-3657-65-R1

FIG. 3 CONFIGURATION OF FLUSH ION PROBES
 (a) 9.5-mm dia
 (b) 0.25×6.3 mm



TB-3857-59

FIG. 3 CONFIGURATION OF FLUSH ION PROBES
 (c) HB-1
 (d) HB-2

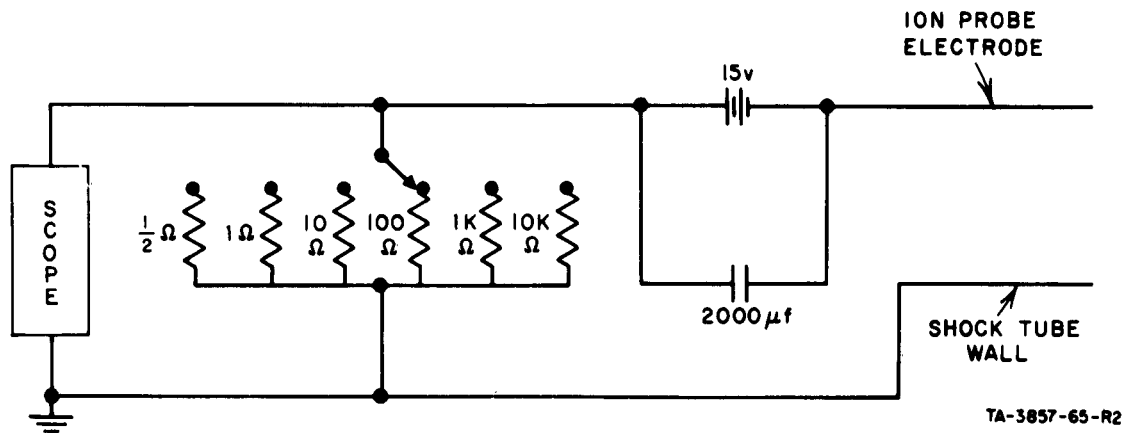


FIG. 4 ION PROBE CIRCUITRY

Typical flush ion probe responses are shown in Figs. 5 through 7. Figure 5 demonstrates the response of the HB-2 probe. The upper trace corresponds to a 0.025-mm (1-mil) diameter wire probe about 1.6 mm above the surface, directly over the flush ion probe. The wire probe axis is perpendicular to the flow. The lower trace indicates the response of the flush ion probe. Note that the flush ion probe follows the wire probe located near the edge of the boundary layer very closely. The current level of the flush probe, when adjusted for probe area differences, is about a factor of six lower than the current level of the wire probe.

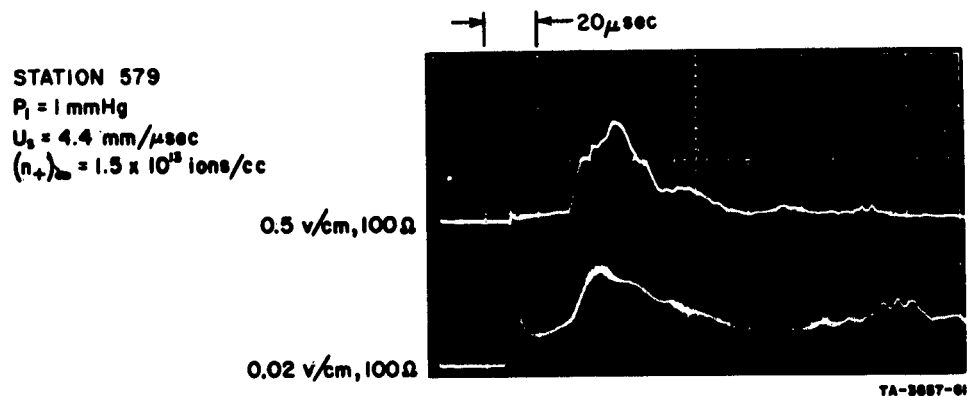


FIG. 5 TIME-RESOLVED RESPONSE OF HB-2 ION PROBE
Upper Trace: Cylindrical Probe 1.5 mm Above Wall Surface
Lower Trace: Flush Probe

Note also the overshoot in the flush probe current at the arrival of the shock front. The velocity boundary layer thickness, 20 μ sec after shock arrival, is about 2 mm.

In Figs. 6 and 7, characteristic flush probe responses to widely differing free-stream conditions are shown. Since all probes indicate similar response characteristics, only the HB-1 probe response is shown in the figures. A typical probe response for intermediate and high free-stream ionization levels is shown in Fig. 6. Note the characteristic current overshoot when the shock arrives. The response of the free-stream ion probe of 0.25-mm diameter and 12.5-mm length is indicated in the same figure. Figure 7 indicates the response of the HB-1 probe to free-stream ion densities about one and one-half orders of magnitude lower (10^{11} ions/cc) than that of Fig. 6. Both the flush probe and the free-stream ion probe

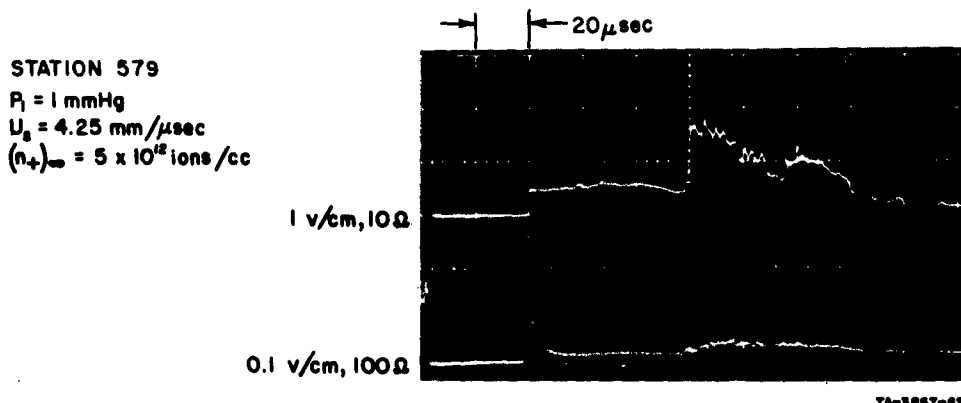


FIG. 6 TYPICAL TIME-RESOLVED RESPONSE OF HB-1 ION PROBE FOR INTERMEDIATE AND HIGH FREE-STREAM ION DENSITIES
 Upper Trace: Free-Stream Probe
 Lower Trace: Flush Probe

show the slow buildup of electron density behind the shock and the overshoot of the flush ion probe is absent. Note that in both figures, corresponding to high and low free-stream electron densities, the flush-mounted ion probes do not indicate a significant increase in response level upon arrival of the interface, while the free-stream probes always exhibit a substantially increased, fluctuating response. Occasionally, depending on free-stream turbulence, the flush ion probes also show the arrival of the contact surface. In such cases, the flush ion probes follow the free-stream probe response closely.

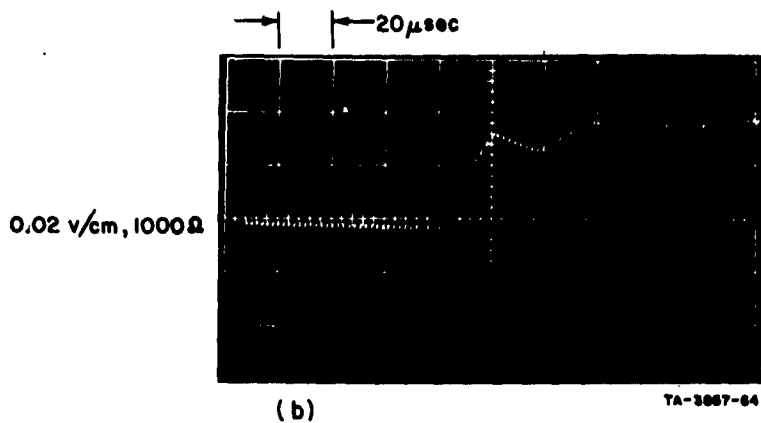
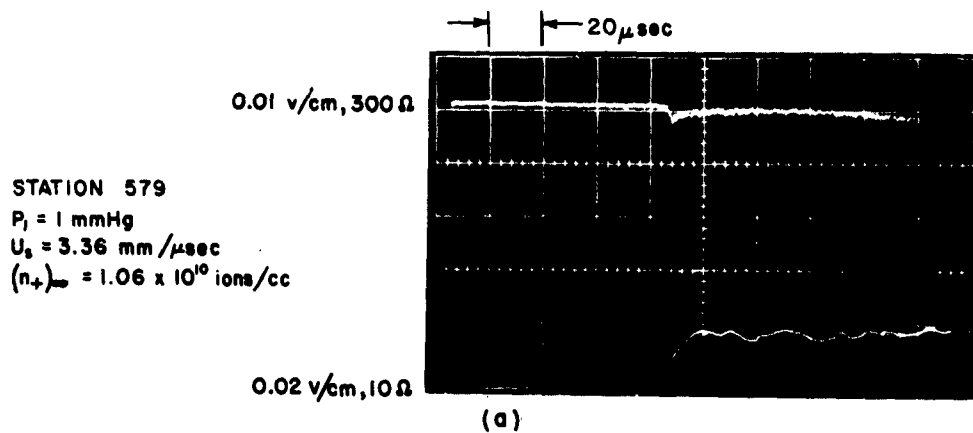


FIG. 7 TYPICAL TIME-RESOLVED RESPONSE OF HB-1 ION PROBE
FOR LOW FREE-STREAM ION DENSITIES

(a) Upper Trace: Photomultiplier
Lower Trace: Free-Stream Probe

(b) Flush Probe

Under turbulent free-stream conditions, as generated by a nonuniform shock wave, the average flush probe response level is substantially increased and exhibits rapid fluctuations (Fig. 8). Compared to a laminar-type probe response for identical theoretical free-stream conditions, the average current level corresponding to turbulent flow is about a factor of two higher.

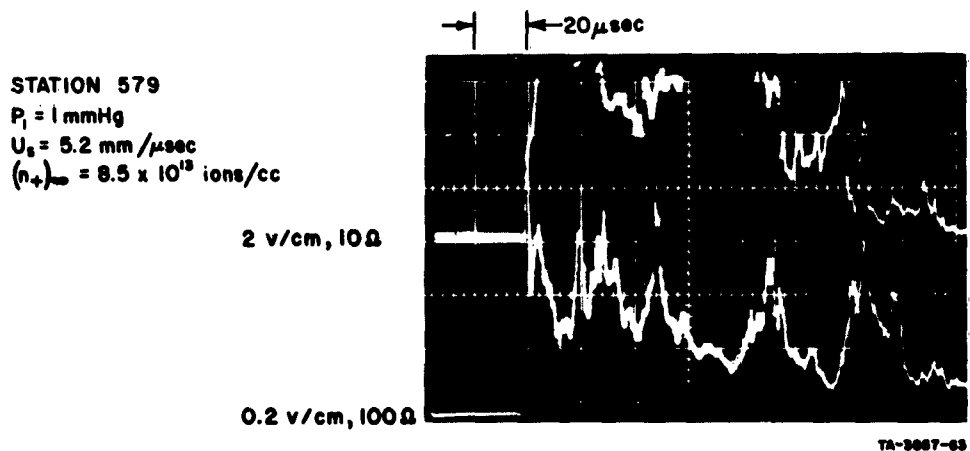


FIG. 8 RESPONSE OF HB-1 ION PROBE TO TURBULENT FREE-STREAM CONDITIONS
 Upper Trace: Free-Stream Probe
 Lower Trace: Flush Probe

The current overshoot on the flush probes is probably related to the absence of a developed boundary layer immediately behind the shock, the translational temperature overshoot, and the ion density incubation times. The overshoot cannot be attributed to the effects of probe capacity, since no significant correlation between probe area and spike level (or between probe area and probe time response) was found. Also, probes covered with a thin coating of dielectric ($\sim 10\mu$) were more than one order of magnitude reduced in response level, and the transient response was significantly shorter than observed with the flush ion probes.

C. RESULTS

The experimental probe current densities have been plotted against the free-stream ion density (or equivalently, shock velocity) in Fig. 9. The theoretical curve appearing in this figure is discussed in Part D of this section. Unless the estimated relaxation distances behind the shock

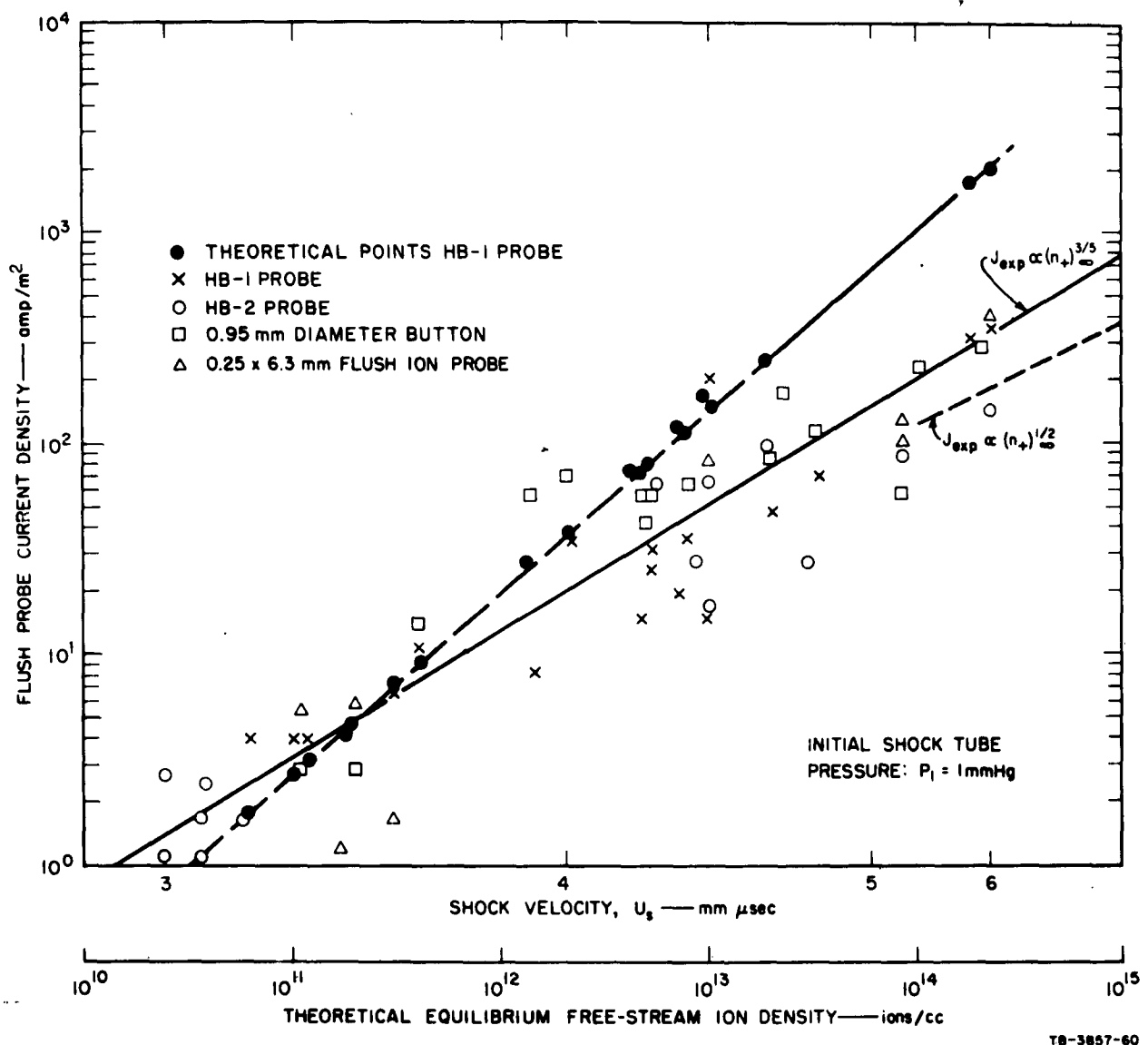


FIG. 9 EXPERIMENTAL AND THEORETICAL FLUSH ION PROBE CURRENT DENSITIES vs. FREE-STREAM EQUILIBRIUM ION DENSITY

front extended further than 10 cm into the test slug,* the data were reduced to the test time corresponding to 10 cm behind the pressure discontinuity.

Interpreting the flush ion probe data on the basis of a zero-order probe theory, described in Sec. D, it was found that the flush probes indicated ion density levels much closer to free-stream values than had initially been expected. The initial estimates were based on the assumption that the cold gas near the wall was in ionization equilibrium. At the low-free-stream ion densities (10^{10} ions/cc), the ion density inferred from flush probe data was a factor of three lower than the corresponding free-stream value. At the higher free-stream ion densities (10^{14} ions/cc), the flush probe data indicated values about an order of magnitude low.

Presumably because of poor experimental conditions in the unsteady boundary layer; i.e., driver impurities deposited on the shock tube wall and turbulent free-stream conditions, the spread in experimental data is about one order of magnitude. However, when observing the variation of test data over four orders of magnitude of free-stream ion density, from (10^{10} ions/cc) to (10^{14} ions/cc), it becomes evident that, for the present experimental conditions, the flush ion probe current level increases with increasing free-stream ion density and is much closer to free-stream values than considerations of ionization equilibrium at the wall would indicate.

If the accumulated data from all probes are considered, the flush probe current varies approximately as

$$J_+ \propto n_+^{3/5}$$

However, a better fit through the HB-1 and HB-2 probe data which covered the widest range of free-stream conditions, would yield

$$J_+ \propto n_+^{1/2}$$

The difference in the power dependence is caused by the fact that the larger (9.5-mm diameter) buttons (used largely at the intermediate free-stream ion densities) seemed to yield higher current densities than Probes HB-1 and

* Here the test slug is defined as the region of shock compressed gas between the shock front and the interface.

HB-2 by about a factor of two. However, no definite conclusion can be made at this time, since this difference in current level is well within the experimental data scatter.

D. CORRELATION WITH THEORY

To check the experimental results, it was necessary to know the variation of the plasma parameters through the boundary layer. It therefore became necessary to investigate, theoretically, the laminar boundary layer problem for the flow of a dissociated gas in a pipe. To obtain a simplified boundary layer solution, a coordinate system fixed with the shock front was chosen to eliminate the time dependence of the boundary layer flow.

Since laminar flow through a pipe before it is fully developed, can be approximated by flow over a flat plate, the problem of a uniform, compressible, dissociated gas flow over flat plate with a sharp leading edge was analyzed. Analysis of a flat plate boundary layer had the additional advantage that many solutions already exist providing a convenient check on the computations.

The general transformed boundary layer equations including a list of symbols is given in Appendix A. These equations must be solved by numerical integration. The general solution for the shock tube case is currently being attempted.

Initially it was thought better to investigate the behavior of a "zero"-order solution. For frozen flow in the boundary layer, a catalytic cold wall, i.e., $z_{+\infty} = 0$, and constant coefficients, the ion mass fraction z_+ is given by Probstein's¹³ relation:

$$z_+ = f'(\eta) = \frac{u}{u_\infty} \quad (10)$$

Since the ion mass fraction is defined as

$$z_+ = \frac{n_+ m_+ / \rho}{[n_+ m_+ / \rho]_\infty}, \quad (11)$$

the boundary layer ion density profile is given by:

$$n_+ = (n_+)_\infty \frac{\rho}{\rho_\infty} \frac{u}{u_\infty} \quad (12)$$

where u is the local x component of velocity, and $f'(\eta)$ is related to the velocity ratio in the boundary layer. The subscript ∞ denotes free-stream conditions. Setting the Lewis number, Prandtl number, and Schmidt number equal to one (these parameters are defined in Appendix A) and assuming constant specific heat and a linearly varying viscosity law, the energy equation becomes identical to the energy equation for undissociated air as solved by Chapman and Rubenstein¹⁶. For a constant wall temperature

$$\frac{T}{T_\infty} = 1 + \frac{\gamma_\infty - 1}{2} M_\infty^2 r(\eta) + a_0 \bar{Y}_0(\eta) \quad (13)$$

and

$$y = \sqrt{\frac{x \mu_\infty C_1}{u_\infty \rho_\infty}} \left[\eta + \frac{\gamma_\infty - 1}{2} M_\infty^2 \bar{r}(\eta) + a_0 \bar{Y}_0(\eta) \right] \quad (14)$$

The functions $r(\eta)$, $\bar{Y}_0(\eta)$, $\bar{r}(\eta)$, $\bar{Y}_0(\eta)$ are given in graphical form in Ref. 16 for $P_r = 0.72$. These functions were recalculated for $P_r = 1$ for the present boundary-layer solutions. Typical normalized curves for the ion concentration profile, velocity profile, temperature, and neutral density profile are shown in Figs. 10 and 11. Since an increase in u_∞ also means increasing the factor $\mu_\infty C$, while γ_∞ and M_∞ are approximately constant, the curves of Figs. 10 and 11 may be used to estimate the boundary layer parameters over the entire range of test conditions covered.

Solving Eq. (8) in Sec. II-D for d_s , one obtains

$$d_s = \left[\frac{9}{8} \epsilon_0 \mu_s \frac{V^2}{J_+} \right]^{1/3} \quad (15)$$

where J_+ is the ion current density and the subscript s denotes variables evaluated as the sheath edge. Since the numerical value for the mobility μ_s depends on the sheath thickness, Eq. (15) must be solved by iteration. However, it is evident from the $1/3$ power in the exponent that d_s is very insensitive to ion mobility and ion current density. Substituting the experimental flush probe current densities for J_+ and estimating the mobility at a point in the boundary layer corresponding to an assumed sheath dimension from the surface, an improved approximation to d_s can be computed. Once the solution for d_s converges to, say, within 20 percent

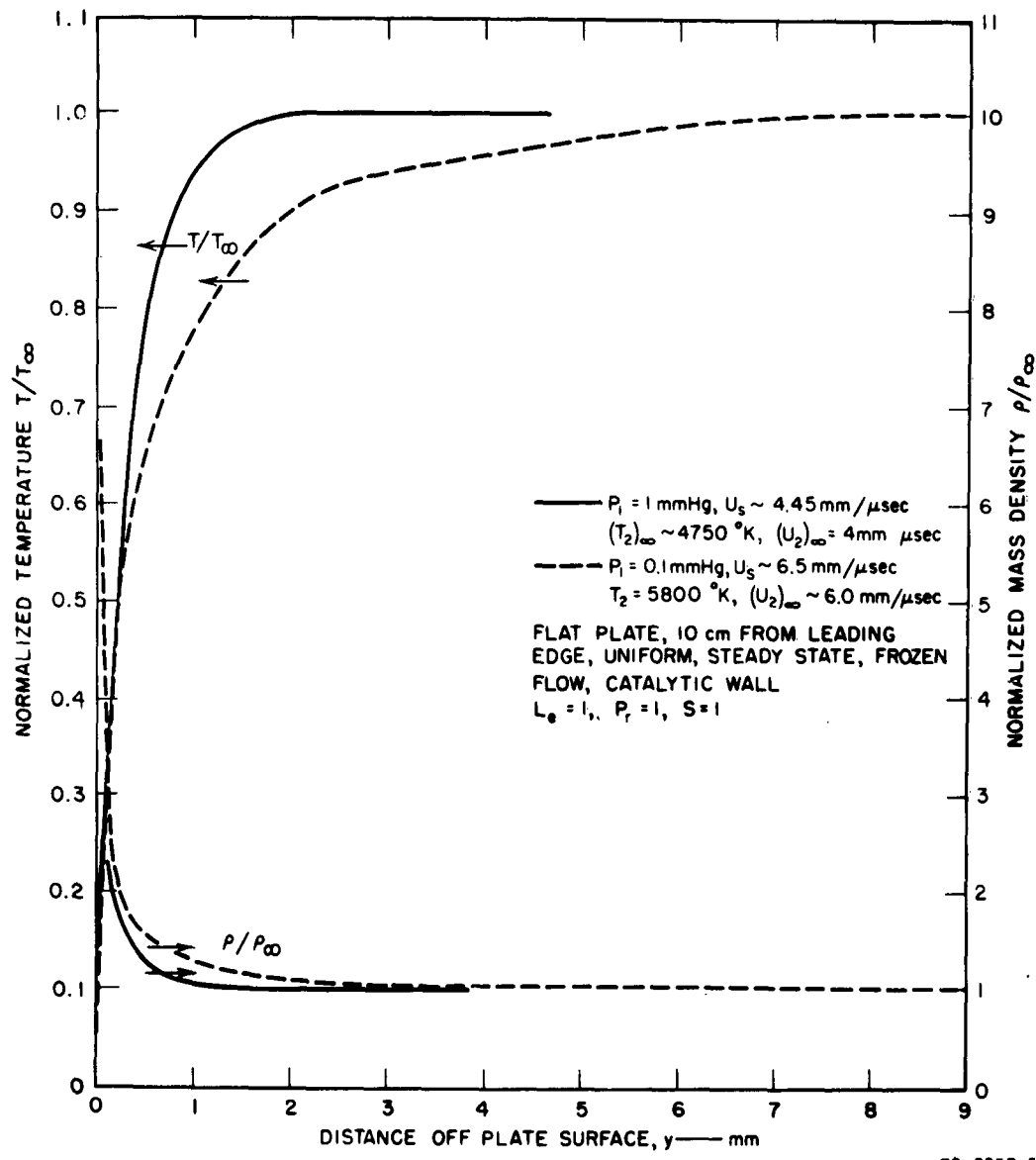


FIG. 10 NORMALIZED TEMPERATURE AND MASS DENSITY PROFILES
THROUGH THE LAMINAR BOUNDARY LAYER ON A FLAT PLATE

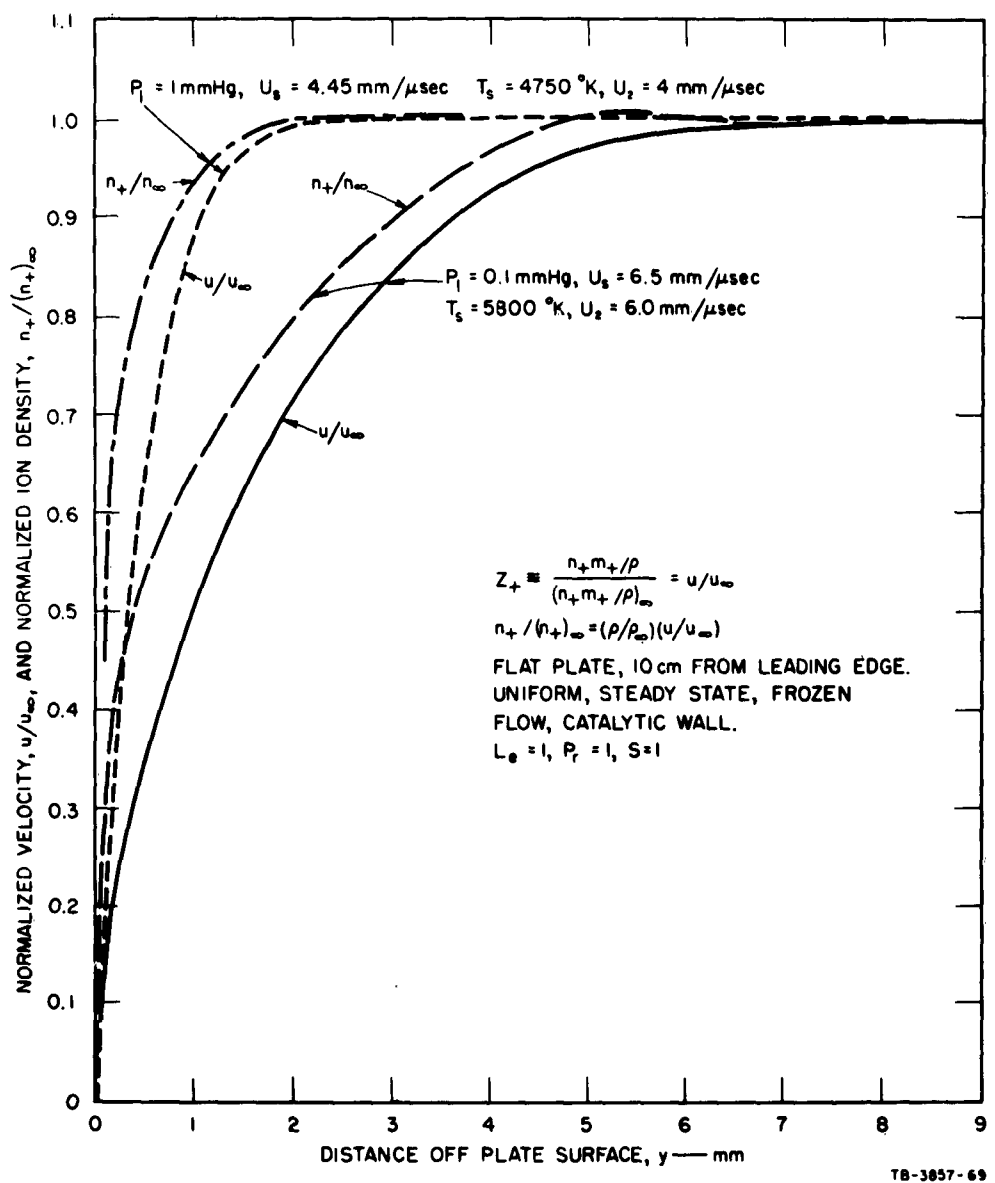


FIG. 11 NORMALIZED VELOCITY PROFILE AND NORMALIZED ION DENSITY PROFILE THROUGH THE LAMINAR BOUNDARY LAYER ON A FLAT PLATE

of the assumed sheath thickness, the approximate sheath thickness has been found. The sheath dimension for the range of experimental conditions tested is shown in Fig. 12. Note that the sheath dimension becomes very large for low free-stream ion densities extending into regions where the ion density at the sheath edge is about one-third that of the free-stream ion density. For high free-stream ion densities, *i.e.*, fast shock velocities, the sheath dimension is very small, extending only to about a tenth of the free-stream ion density. These predictions have been qualitatively verified by the current densities obtained in the flush probe experiments.

For a given sheath dimension, values of $(n_+)_s$ and $(V_{th})_s$ can be obtained from the theoretical boundary layer profiles for normalized ion density and temperature. Thus theoretical current density estimates can be obtained from Eq. (9):

$$J_{+s} = \frac{(n_+)_s (V_{th})_s e}{4} \quad (16)$$

and compared to experimentally obtained current density estimates. The curve for theoretical current density estimates has been superimposed on the experimental data in Fig. 9. The data points on the theoretical curve correspond to sheath dimensions obtained from the HB-1 probe data. Note that despite all assumptions made in the zero-order boundary layer theory and probe theory, the agreement between theoretical predictions and experimental data is surprisingly good. There is, however, a disagreement in the power-law dependence between the experimental and theoretical current relations. The difference in slope is probably due to the mathematical restrictions on transport parameters, frozen flow condition, etc. *A priori*, there is no physical reason why the free-stream ion density-flush probe current density relation should be a straight line on the log-log paper.

As expected, agreement is best at the low shock velocities, where the degree of ionization is low, while at the high velocities the approximations regarding the transport parameters and the frozen flow condition deteriorate.

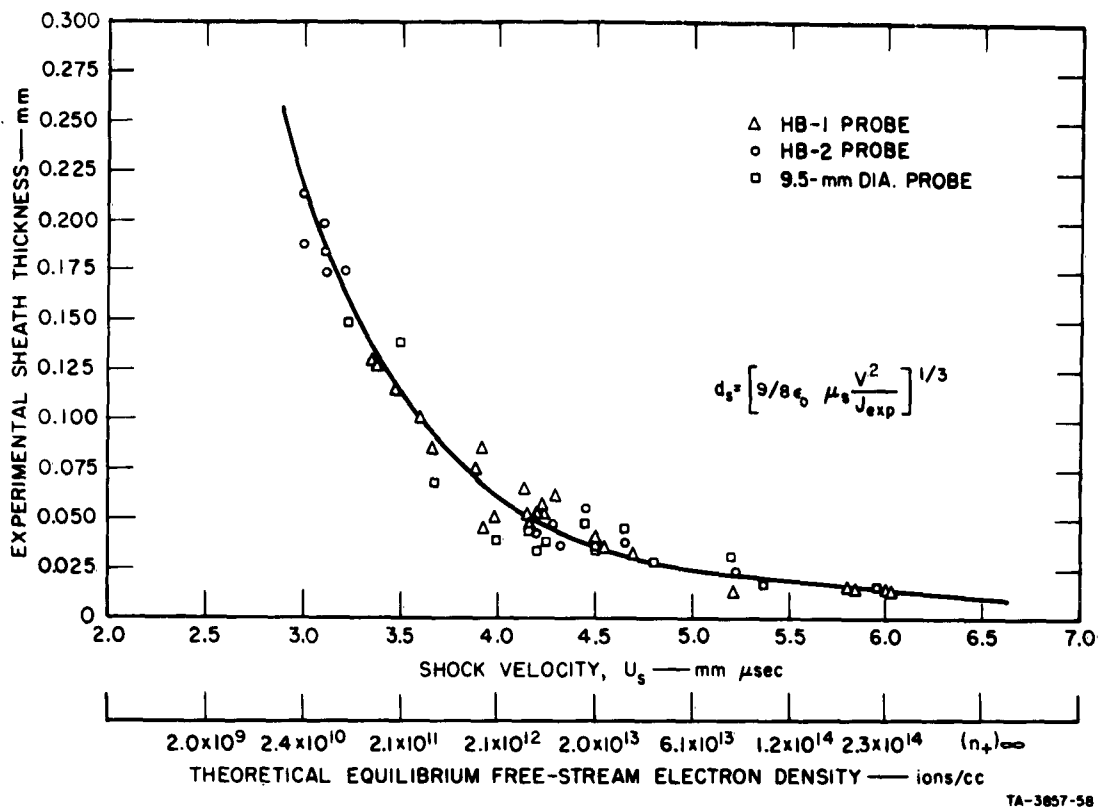


FIG. 12 EXPERIMENTALLY DETERMINED COLLISION-DOMINATED SHEATH THICKNESS FOR FLUSH ION PROBE vs. FREE-STREAM ION DENSITY

E. SUMMARY AND CONCLUSIONS

Over the range of free-stream conditions covered, from 10^{10} to about 10^{14} ions/cc, it was found that the flush-mounted ion probes sample the ion density existing at the probe sheath edge. Interpreting the probe current as $J_+ = n_+ e v_{th} / 4$, at the low free stream ion density levels, the flush mounted ion probes measure ion density about a factor of three lower than free stream values. For high free stream ion densities, the probes indicated ion densities about one order of magnitude reduced from free-stream levels. These results agree well with theoretical expectations based on boundary layer ion density profiles and sheath dimensions computed by means of the collision dominated, space charge limited diode equation. In addition, considerations of probe theory indicate another means of obtaining boundary layer ion density profiles from flush probe data. Equation (15) shows that d_s has a strong dependence on the probe

potential. Thus, if the probe sheath can be varied by modulating the probe potential, it may be possible to obtain the ion density profile in the boundary layer.

F. FUTURE WORK

Since the flush probe environment on actual re-entry vehicles is extremely complex, the experimental environment has been simplified in the present study of flush probe operation. For the simplified test conditions the variation of the probe parameters through the boundary layer becomes calculable and the effects of various parameters can be isolated and studied separately.

For a flat plate with a sharp leading edge, suspended in a uniform, high-velocity, highly dissociated free stream, the differential boundary layer equations reduce to a relatively simple form and numerical integration is not too difficult. Accordingly, the next phase of this work will be primarily concerned with flush ion probe operation on flat plates. In addition, whenever possible, the theoretical boundary layer calculations will be checked experimentally, by measuring the boundary layer ion density profile thin-wire probes.

The future experimental program, as it is presently planned, can be described as follows:

- (1) Determine flush probe response on the plate over a wider range of free-stream ion densities.
- (2) Determine probe response associated with frozen (as opposed to near-equilibrium) flow. These parameters can be evaluated in the shock tube by changing the initial shock tube pressures.
- (3) Determine the variation in probe response due to changing the applied battery voltage. This also will provide a check on the probe theory.
- (4) Experimentally determine ion density profiles in the boundary layer.
- (5) Determine boundary layer electron temperatures.

Currently, experimental work on Steps (1), (2), and (4) is in progress. The current tests are being conducted at 0.1 mmHg initial shock tube pressures, covering a range of shock Mach numbers from $M_s = 16$ to $M_s = 24$. The flat plate probe configuration currently being used is

shown in Fig. 13. Wires about 0.025-mm in diameter are spaced at various distances from the flat plate surface, separated laterally to minimize probe interactions. The diameters were selected so that the probes are in a free molecular regime with respect to the neutral gas. To avoid disturbing influences from the thicker support posts, the ends of the wires are insulated. A flush-mounted probe is located at the center of the plate. All probes are operated as unequal area probes.

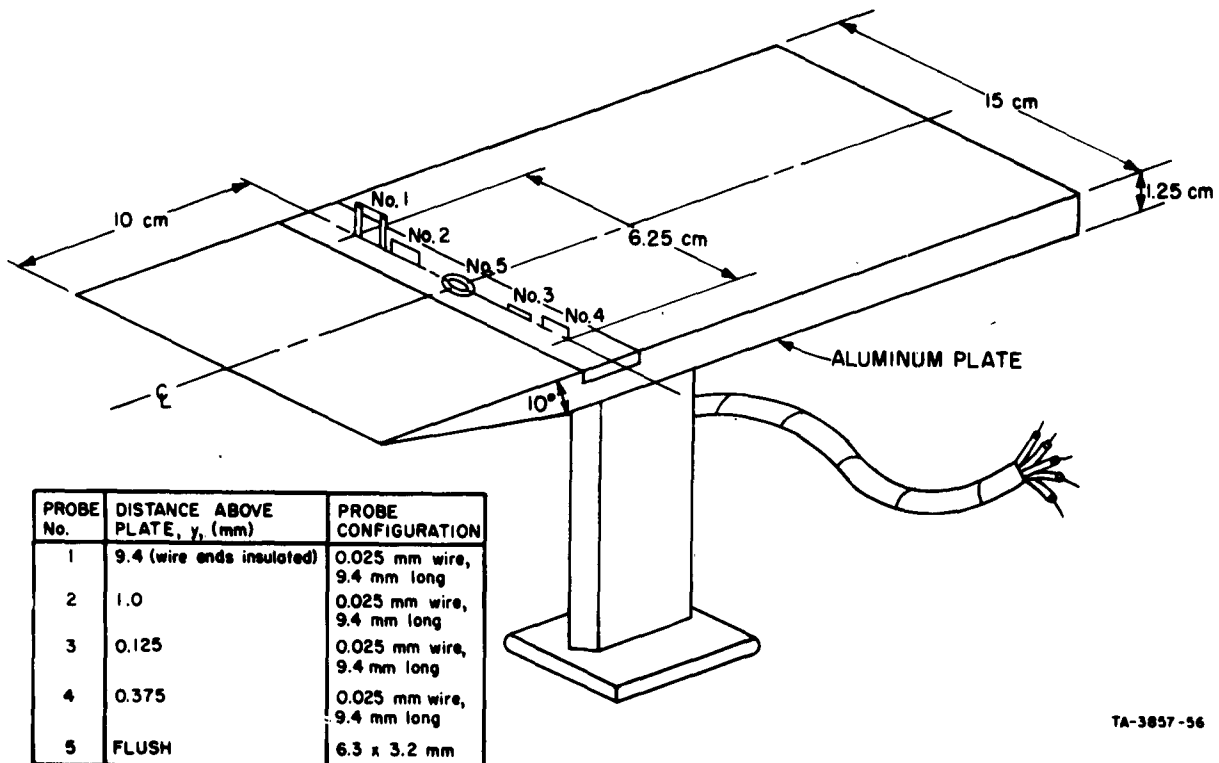


FIG. 13 EXPERIMENTAL ARRANGEMENT OF CYLINDRICAL ION PROBES AND FLUSH PROBES ON A FLAT PLATE TO MEASURE ION DENSITY PROFILE THROUGH THE BOUNDARY LAYER

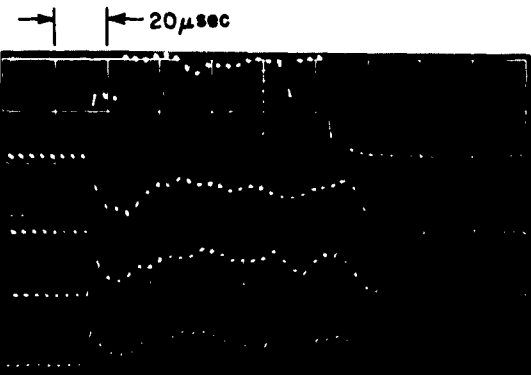
Figure 14 indicates the nature of response from the boundary layer probes. Note that small perturbations occurring in the records appear at the same time on all probes. Also, note that the current level fluctuations are small.

9.4 mm OFF SURFACE
5 v/cm, 1000 Ω

1 mm OFF SURFACE
5 v/cm, 1000 Ω

0.375 mm OFF SURFACE
2 v/cm, 1000 Ω

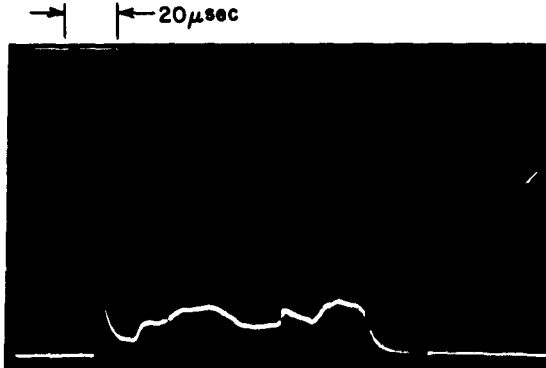
0.125 mm OFF SURFACE
2 v/cm, 1000 Ω



(a)

STATION 1093
 $U_s = 6.2 \text{ mm}/\mu\text{sec}$
 $P_i = 0.1 \text{ mmHg}$
 $(n_+)/_{\infty} = 1.8 \times 10^{18} \text{ ions}/\text{cc}$

0.186 cm² PROBE AREA
0.25 v/cm, 100 Ω



(b)

TA-3687-66

FIG. 14 CHARACTERISTIC ION PROBE RESPONSES

(a) Probes above Plate Surface

(b) Flush Probe

The above currents have been reduced to ion density values and are shown in Fig. 15 superimposed on the theoretical boundary layer profiles. Note that the agreement between theoretical and experimental ion density profile is good. The preliminary result should be viewed with caution, however, since it represents only a single experimental condition.

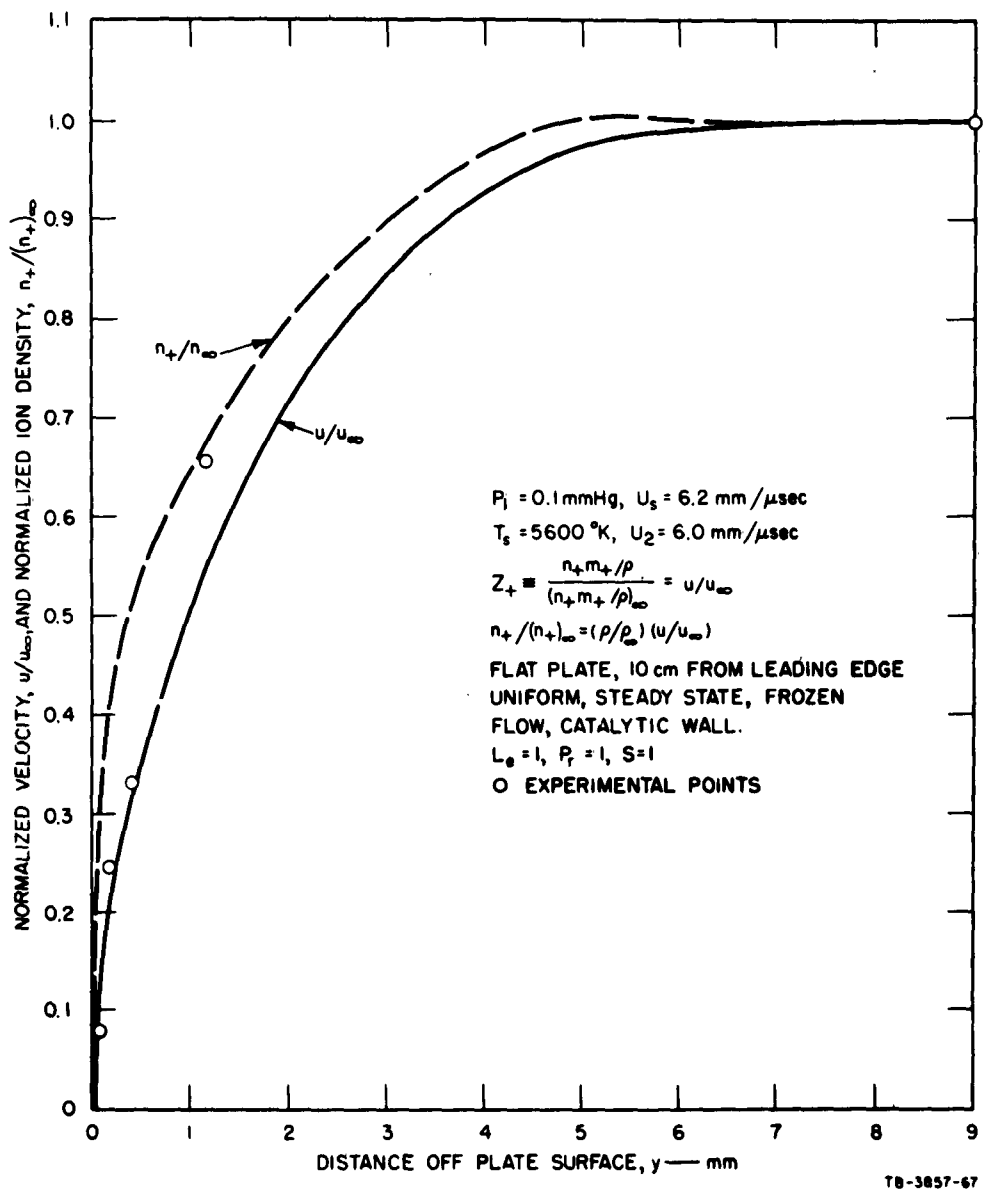


FIG. 15 REDUCED EXPERIMENTAL DATA FOR FIG. 14 SUPERIMPOSED
ON NORMALIZED THEORETICAL BOUNDARY LAYER ION DENSITY PROFILE

IV PRECURSOR MEASUREMENTS

The occurrence of precursor ionization phenomena associated with strong shock waves in air and in the noble gases has been reported by several investigators.¹⁴⁻¹⁶

To verify these reports, experiments have been performed in the arc-driven shock tube at high shock velocities, *i.e.*, M_s = 15 to 22, with room air and at 0.1 mmHg initial shock tube pressures. The experiments used a free-stream cylindrical ion probe 1.5 mm in diameter. The probe radius was of the order of a free-stream mean free path ahead of the shock.

A typical ion probe response is shown on the lower trace of Fig. 16. It is interesting to note that the rate of increase in signal level becomes very large a short distance ahead of the shock front. At about 6 to 10 μ sec (7 cm) ahead of the pressure discontinuity, the signal is driven off scale.

The reduced data, adjusted for probe sheath dimensions, are presented in Fig. 17. The bars denote the extent of data scatter. For reference, the corresponding equilibrium slug electron densities are also shown on the graph.

To verify the precursor ionization profiles obtained from ion probes and to discriminate against possible probe surface photoelectric effects,

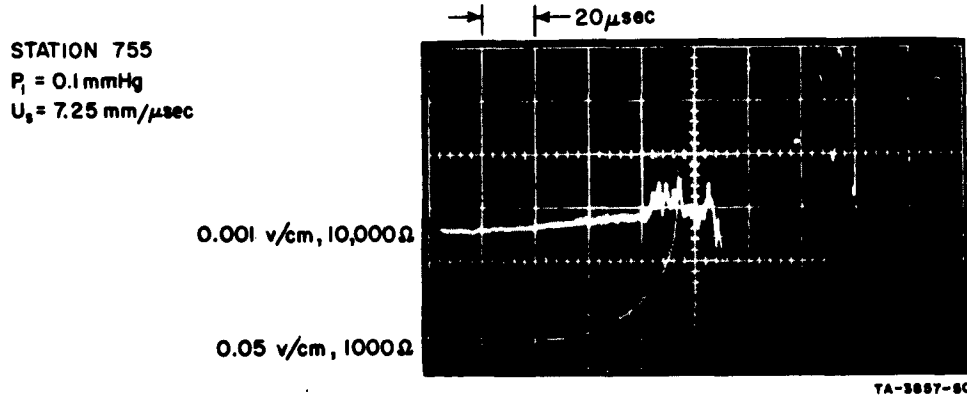


FIG. 16 TIME-RESOLVED MICROWAVE INTERFEROMETER AND ION PROBE RESPONSES FROM IONIZATION PRECURSOR MEASUREMENTS
Upper Trace: 3.3 Gc Microwave Interferometer
Lower Trace: Free-Stream Probe (1.5-mm diam \times 16 mm long)

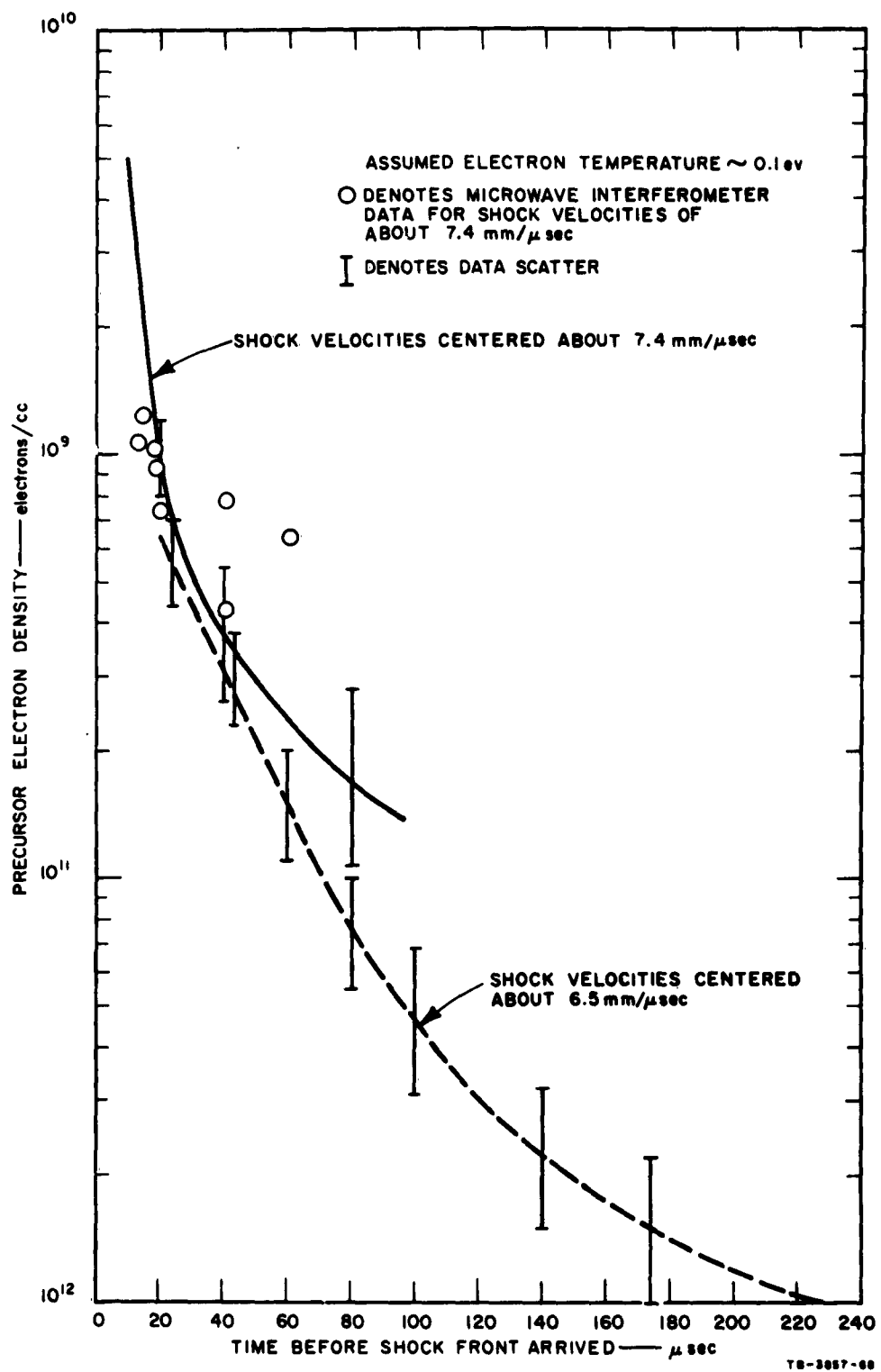


FIG. 17 MEASURED PRECURSOR IONIZATION PROFILES IN AIR AHEAD OF THE SHOCK FRONT

a few experiments were repeated using a 33-Gc microwave interferometer. The interferometer actually had been set up to measure test slug equilibrium electron densities so that the sensitivity was only marginal for the precursor measurements. A characteristic precursor microwave interferometer response is shown in the upper trace of Fig. 16. Note that while the deflection is small, it is observable up to about 100 μ sec ahead of the shock wave. To reduce the probe data, the temperature of the precursor electrons has been assumed equal to 0.1 ev. The reduced microwave data have been superimposed on the ion probe data of Fig. 17. Comparison of the inferred electron densities as given by the microwave system with those inferred from ion probe measurements show agreement to within a factor of two. A more sensitive interferometer is presently being constructed to resolve the electron density profile in the precursor.

The effect of photoemission from the probe surface on the probe response has been examined by enclosing the ion probe in a thin dielectric sheath (wall thickness = 0.3 mm). Unless the photoemissive properties of the dielectric and metallic materials are identical, the current response of the dielectric-covered ion probe to the precursor should change. If the current is not produced by the emission of photoelectrons but by a plasma of charging electron density, then the covered-probe and bare-probe current responses should be the same (the capacity of the dielectric is very large compared to the capacity of the plasma sheath; hence, there is negligible voltage drop across it as the electron density increases). Indeed, the bare and dielectric-covered ion probe currents were found to be identical. The photoemissive properties of the dielectric material (modified polyvinylchloride) are unknown, but assuming they are not identical to those of the metal conductor, the comparative current measurements indicate that photoelectron current is negligible.

The present results indicate electron densities of the order of 10^9 electrons/cc about 10 cm ahead of the shock front. Verification of the precursor ionization is important, since it shows that radar cross section of blunt bodies can be markedly increased at VHF frequencies.

In the future, it is planned to measure the electron temperature in the precursor by a Langmuir probe technique and to measure the approximate distribution of nonequilibrium shock front radiation (assumed to be causing the precursor ionization) by utilizing the photoelectric effect of certain metal surfaces¹⁷ and a field of view perpendicular to the direction of motion.

V RVIP FLIGHT TEST CALIBRATIONS

Recently, Langmuir probes have been flown on the Re-Entry Vehicle Instrumentation Program (RVIP) in an effort to measure the electron concentration around vehicles re-entering the earth's atmosphere.²⁷ The initial flight results indicate that the inferred electron density is about an order of magnitude less than the inferred ion density and that the inferred electron temperature was about twice the value expected. In an effort to resolve some of the flight data anomalies, laboratory calibration of the RVIP probes was undertaken. The laboratory measurements have been performed in an electromagnetic shock tube and in a thermally generated plasma. The environment for the laboratory measurements was such that the mean free path was much greater than either the probe radius or the sheath thickness; hence, the classical theory of Langmuir is applicable.

A. MEASUREMENTS

Three aspects of probe performance are to be checked in this calibration program. It is desired to determine the applicability of Langmuir probe theory to the determination of electron and ion density as well as electron temperature. To measure the electron and ion saturation current characteristics, the electromagnetic shock tube (described in Appendix C), was considered most suitable because of its ability to reproduce a plasma at low pressures (long mean free paths). To perform the measurement of electron temperature, a seeded low-pressure flame was deemed most appropriate because of the long test times available. Details of the low-pressure flame facility are given in Appendix C.

1. GENERAL ELECTRIC PROBE

Figure 18 shows one of four sensing tips of the probe designed by General Electric mounted on a support column, which also serves as the reference electrode. A single sensing tip and the column serve as a Langmuir probe. The area of the reference electrode is 2,500 times the area of the sensing tip. The sensing tip has a dimension of $3(10^{-2})$ cm and an area of $4.2(10^{-7})$ m².

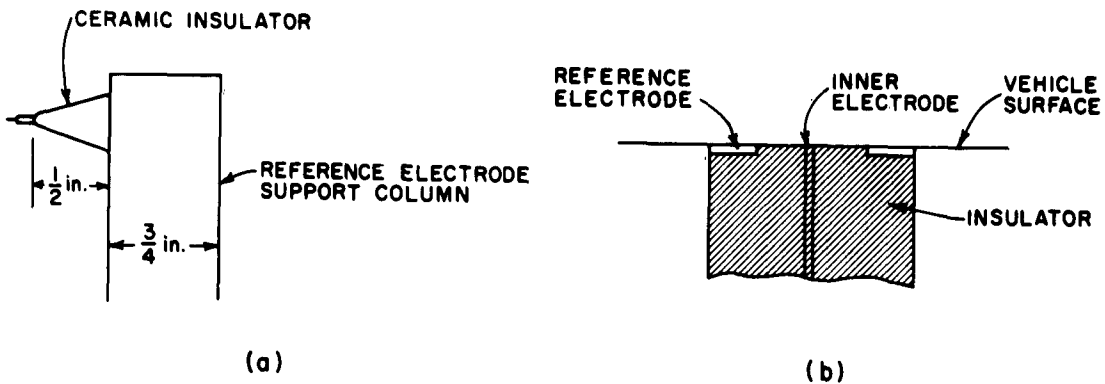


FIG. 18 RVIP PROBE GEOMETRIES USED IN CALIBRATION
 (a) General Electric Probe
 (b) AVCO Probe

TA-3057-18

The General Electric probe is designed to sample the high-altitude (300,000 ft) shock formation about a re-entering vehicle. As a consequence, the electron density regime of interest is between 10^7 and 10^9 electrons/cc. In this electron density regime, the sheath thickness is much greater than the characteristic probe dimension. The details of electrode geometry (i.e., whether the electrode is a cube or a sphere) are thus unimportant and the electrode is assumed to be spherical for analytic purposes. (The theory for the collection of charge by a spherical probe was considered in Sec. II-A.)

Figure 19 is a plot of ion density as a function of ion saturation current for an electron temperature of 5000°K and a normalized electrode voltage, $\eta = eV/kT$, of 20. The solid lines of Fig. 19 represent the asymptotic limits of current for probe radius much greater than or much less than ($\eta < a/r_p$) the sheath radius. The open circles are calculated points using the theory of Allen *et al.*,⁵ and the dashed line is a straight-line approximation joining the asymptotic solutions through the open circles.

The General Electric probe was placed in the electromagnetic shock tube and biased for ion collection. (Ion density can be inferred from measurements of the current density on the probe as the shock passes the probe.) The ion density at the instant of shock passage, as well as 400 μsec and 5 msec after the passage of the shock front, was inferred from curves such as that of Fig. 19. The density inferred from these

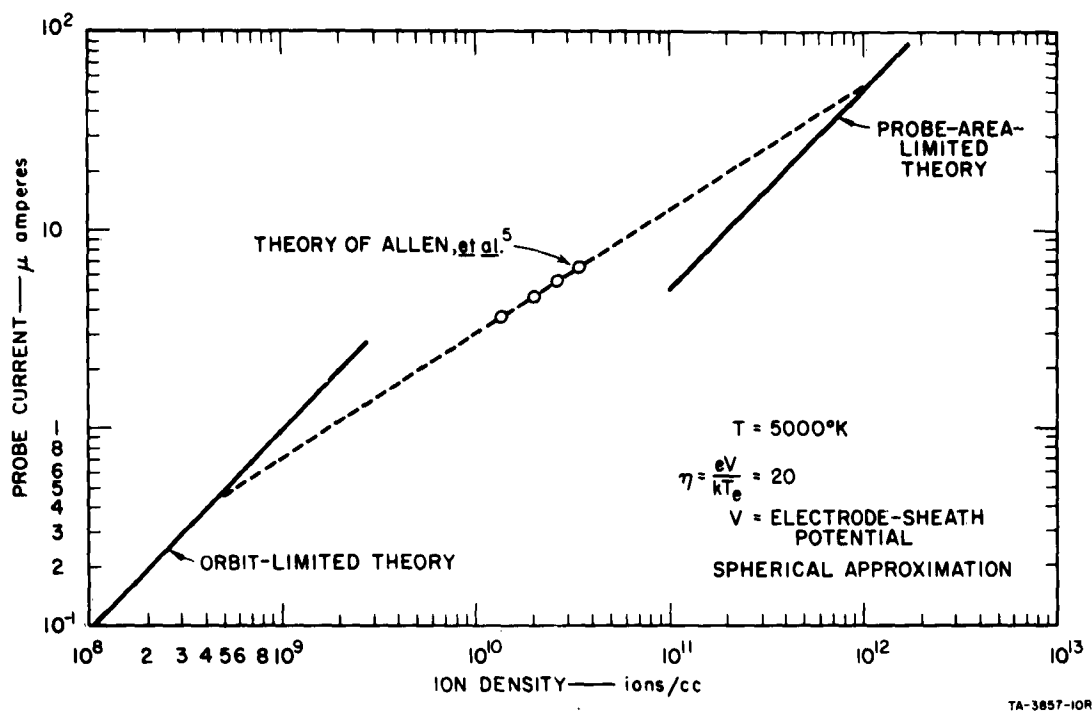


FIG. 19 ION DENSITY AS A FUNCTION OF ION SATURATION CURRENT FOR THE GENERAL ELECTRIC PROBE

measurements was checked against the values measured by a cylindrical probe, which had been previously calibrated against a microwave transmission measurement. Over a range of ion density from 10^7 to 10^9 ions/cc, the probes were in agreement to a factor of two, as shown in Fig. 20.

When the SRI calibration probe and the RVIP probe were biased for the measurement electron density in the shock tube, the inferred electron density was an order of magnitude lower than the inferred ion density. As noted previously, the error in electron density estimates is frequently observed and further investigation is required.

A full Langmuir (current voltage) characteristic of the General Electric probe, taken in a seeded flame, is shown in Fig. 21. The inferred electron temperature from the slope of the characteristic is 4000°K , a number that is a factor of two higher than the estimated temperature of the flame. (A similar result is obtained from the calibration probe.) For this case, the ratio of the inferred electron and ion density is within a factor of two of unity, however this ratio does vary with electrode voltage. It should be noted that the plasma environment of the

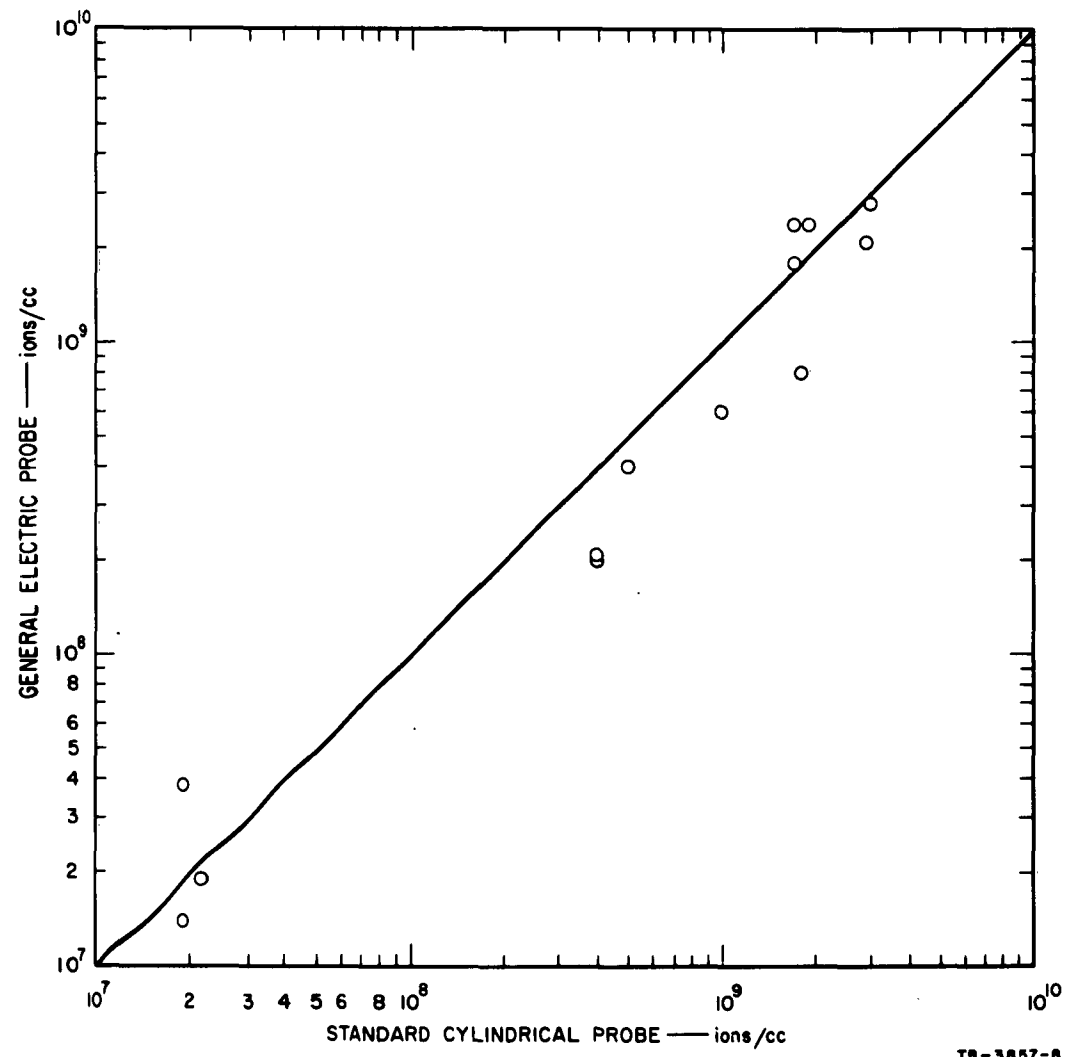
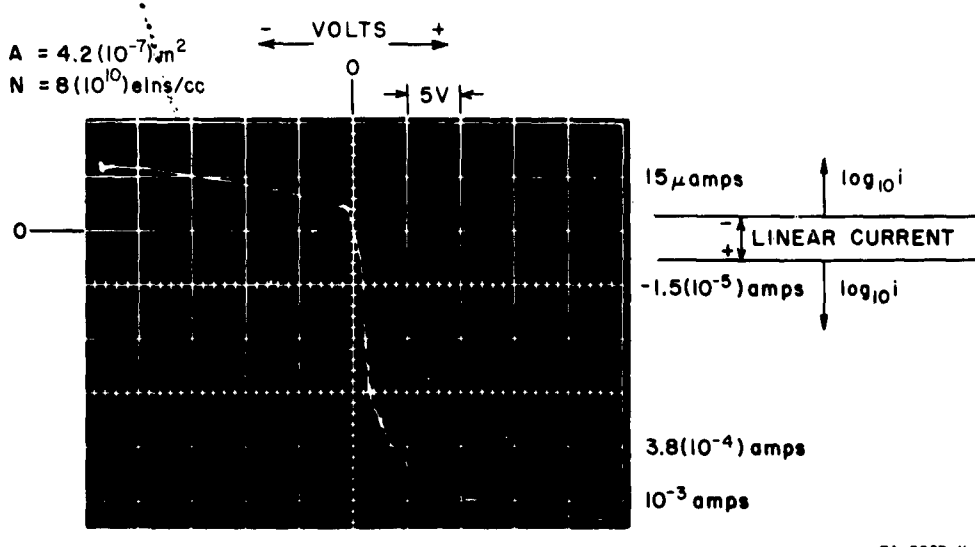


FIG. 20 ION DENSITY INFERRED FROM GENERAL ELECTRIC PROBE
vs. DENSITY MEASURED WITH STANDARD PROBE



TA-3887-II

FIG. 21 LANGMUIR CHARACTERISTIC OF GENERAL ELECTRIC PROBE IN THE FLAME FACILITY

seeded flame is free of electric and magnetic fields, in contrast to the environment of the electromagnetic shock tube. In addition, the ionization is thermal and in equilibrium in the flame, a situation that does not obtain in the shock tube.

2. AVCO FLUSH-MOUNTED LANGMUIR PROBE

Figure 21(b) shows the coaxial geometry of the Langmuir probe designed by AVCO for the RVIP program. This probe is designed to be mounted flush to the re-entry vehicle surface. A probe having the same geometry (but slightly different dimensions) of that of Fig. 21(b) was tested in the electromagnetic shock tube.

When the probe's inner conductor was biased negatively for ion collection, the inferred ion density agreed within a factor of two with the measured ion density inferred from a calibration probe, provided that the collecting area of the flush probe is taken to be the surface area of the sheath. The sheath thickness, d_s , is approximated by

$$d_s \sim \lambda_D^{3/4}$$

At high ion densities, when the sheath thickness is smaller than the diameter of the inner conductor, d , the area for ion collection is just the physical area of the probe, or $(\pi d^2/4)$. At low ion densities, when $d_s > d$, the collecting area can be approximated by the surface area of the sheath, or $(\pi d_s^2/2)$.

When the inner conductor was biased positively for electron collection, the inferred electron densities were too low compared with the previous estimates of the electron density. This observation is in agreement with the previous measurements.

One difficulty arising from the geometry of the AVCO probe is its vulnerability to leakage currents, thereby limiting instrument sensitivity. The electrode area is very small. At low altitude, when the vehicle surface is hot, the leakage current across the lossy dielectric can quite possibly exceed the current collected by the electrode, particularly at low electron density levels.

B. CONCLUSIONS AND RECOMMENDATIONS

On the basis of these measurements, it is concluded that

- (1) Determination of ion density from the RVIP probes is within a factor of two of the actual density when the classical Langmuir theory is applicable.
- (2) Estimates of electron density from the RVIP probes are questionable. This conclusion is a result of a comparison of inferred electron and ion densities with the electron density measured by microwave techniques. In these measurements, the observed electron density can be as much as an order of magnitude too low.
- (3) Estimates of the electron temperature from the RVIP probe data are no better than a factor of two under ideal conditions. It is anticipated the accuracy of the temperature measurement will suffer when the electron density estimates differ significantly from those of the ion density. In any case, it would be extremely desirable to record the entire current-voltage characteristic.

An examination of the initial probe measurements on the LORV program has led to the following recommendations:

- (1) The size of flush probe electrode area should be increased. A possible configuration requiring a minimum

of system changes is that probe being used in a joint program involving Sperry-AVCO-SRI. (A sketch of the configuration of this probe is shown in Fig. 22.) Increasing size will

- (a) simplify interpretation of probe currents;
- (b) allow measurements at high altitudes;
- (c) make the probe less vulnerable to leakage currents.

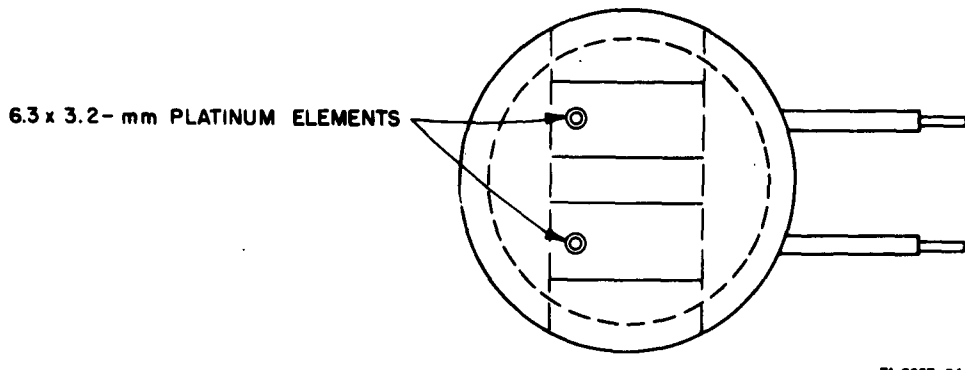


FIG. 22 SPERRY FLUSH-MOUNTED PROBE

- (2) Increase the voltage swings on the electrostatic probe sweeping circuitry beyond the present ± 4 to at least ± 10 volts. The probe may not be reaching saturation electron current.
- (3) Operate at least one of the probes with a constant voltage bias. A suitable bias voltage would be -10 v, so that probe continuously measures ion current. This will make the probe less susceptible to instrumentation difficulties.
- (4) The electrostatic probe electronics should be checked out in a plasma environment, to check for any peculiarities introduced into the results when the instrumentation is operated with a nonlinear load.

APPENDIX A

GAS-DYNAMIC BOUNDARY LAYER THEORY

APPENDIX A

GAS-DYNAMIC BOUNDARY LAYER THEORY

1. INTRODUCTION

In the shock tube, the flat plate boundary layer is so highly cooled (constant room temperature wall conditions) that (after steady state is established) the presence of atoms and ions in the boundary layer is only due to diffusion from the free stream. In fact, under complete temperature equilibrium conditions, the charge density in the vicinity of the shock tube wall would always be equal to zero. Considering the computational difficulties associated with the analysis of a non-equilibrium multicomponent gas mixture it is hoped that, for the shock tube conditions, the simpler boundary layer equations using a binary gas and average gas mixture properties will yield useful approximations to the charge density profiles in the boundary layer.

The following general assumptions apply:

- (1) The gas is only slightly ionized.
- (2) All gas species can be considered to behave as perfect gases.
- (3) The flow is in a steady state.
- (4) Uniform, parallel, flow over a flat plate is considered, *i.e.*, the flow is two-dimensional, and all free-stream gradients in the x direction are equal to zero.
- (5) The effect of a boundary layer induced oblique shock over the plate is negligible.
- (6) The plate temperature remains constant at the room temperature level, *i.e.*, the plate does not heat up in the short test times considered.
- (7) Radiation effects are ignored.

Since most of the theory used here has been developed in Refs. 18 through 20, only major steps are repeated to point out the pertinent assumptions.

The following symbols are used:

a = speed of sound

C = Nondimensional density-viscosity product = $(\rho\mu/\rho_\infty\mu_\infty)$

C_1 = $\sqrt{T_\infty/T_\infty} [(T_\infty + S)/(T_\infty + S)]$ = constant of proportionality in the absolute viscosity temperature relation.

c_i = mass fraction of component i

c_+ = mass fraction of ions

$c_{p,i}$ = specific heat per unit mass at constant pressure of component i

\bar{c}_p = average specific heat per unit mass at constant pressure for the gas mixture, defined by Eq. (A-11)

D_{12} = binary diffusion coefficient for atom-molecule gas mixture

D_a = ambipolar diffusion coefficient

g = normalized enthalpy parameter in the boundary layer

h = enthalpy per unit mass of mixture

h_i = perfect gas enthalpy per unit mass of component i , defined in Eq. (A-9)

h_i° = heat evolved in the formation of component i at 0°K per unit mass

h_o = total enthalpy defined in Eq. (A-7)

k = thermal conductivity

l = significant dimension, distance from plate leading edge

L = Lewis number for atom-molecule mixture = $(\rho D_{12} \bar{c}_p / k)$

M = Mach number = U/a

\bar{m} = molecular weight of mixture

m_+ = molecular weight of ion

m_- = molecular weight of electrons

n = neutral particle number density

n_+ = ion number density

n_- = electron number density

p = pressure

P_r = Prandtl number = μ/kc_p

R_e = Reynolds number = $Ul\rho/\mu$

S = Schmidt number = $\mu/\rho D_{12}$
 S_a = Schmidt number based on ambipolar diffusion coefficient
 s = boundary layer parameter defined by Eq. (A-15)
 T = absolute temperature
 u = x component of velocity
 v = y component of velocity
 w_i = net mass rate of formation of component i per unit volume and time
 x = distance along plate
 y = distance normal to surface
 z_i = normalized mass fraction of specie i
 z_t = normalized mass fraction ions
 η = boundary layer parameter defined by Eq. (A-16)
 μ = absolute viscosity
 γ = ratio of specific heat
 ρ = mass density
 ψ = stream function defined by Eq. (A-12)

SUBSCRIPTS

∞ = denotes free stream conditions, external to the boundary layer
 w = wall
 i = i th component of the mixture

2. BOUNDARY LAYER EQUATIONS:

a. EQUATION OF CONSERVATION OF SPECIE

If it is assumed for a slightly ionized gas, that charge diffusion can be described by a process similar to chemical specie diffusion, and if in addition, the assumption of a binary gas is made, the conservation equation for the ion mass fraction becomes:

$$\rho u \frac{\partial c_+}{\partial x} + \rho v \frac{\partial c_+}{\partial y} = \dot{w}_+ + \frac{\partial}{\partial y} \left(\rho D_a \frac{\partial c_+}{\partial y} \right) \quad (A-1)$$

where

$$c_+ = \frac{n_+ m_+}{n m} = \frac{n_+ m_+}{\rho} \quad n_+ \ll n \quad (A-2)$$

and, since,

$$n_+ m_+ \gg n_- m_- \quad , \quad (A-3)$$

$$n_+ m_+ + \sum_i n_i m_i = \bar{n} \bar{m} \quad \text{where the summation is over all neutral atoms and molecules}$$

Here D_a is the ambipolar diffusion coefficient, and the two-component gas is considered to be made up of neutrals and charged particles. Inherent in the above equation is the assumption that pressure and temperature diffusion gradients are small compared to specie concentration gradients.

Summing over all specie, the equation for conservation of mass becomes

$$\frac{\partial(\rho u)}{\partial x} + \frac{\partial(\rho v)}{\partial y} = 0 \quad . \quad (A-4)$$

b. EQUATION OF MOTION

The momentum equation for uniform two-dimensional flow over a flat plate becomes:

$$\rho u \frac{\partial u}{\partial x} + \rho v \frac{\partial v}{\partial y} = \frac{\partial}{\partial y} \left(\mu \frac{\partial u}{\partial y} \right) \quad . \quad (A-5)$$

In this equation, the assumption has been made that the viscous dissipation gradients in the x direction, within the boundary layer, and the viscous contributions from the induced y component of velocity are of second order.

c. ENERGY EQUATION

Since it was assumed that the gas is only slightly ionized, the fractional amount of energy contained in the ionization mode is negligible and therefore, the ionization recombination process itself cannot influence the temperature or enthalpy profiles to a large extent. This assumption leads to the uncoupling of the species conservation and energy equation, i.e., the variable transport coefficients may be assumed to be independent of each other in the two equations. The energy equation is therefore written on the basis of a binary gas made up only of neutral atoms and molecules.

In terms of enthalpy:

$$\rho u \frac{\partial h_0}{\partial x} + \rho v \frac{\partial h_0}{\partial y} = \frac{\partial}{\partial x} \left[\frac{\mu}{P_r} \frac{\partial h_0}{\partial y} + \mu \left(1 - \frac{1}{P_r}\right) \frac{\partial(u^2/2)}{\partial y} \right] - \frac{\partial}{\partial y} \left[\left(\frac{1}{L} - 1 \right) \rho D_{12} \sum_i c_i \frac{\partial c_i}{\partial y} \right] \quad (A-6)$$

where

$$h_0 = h + \frac{u^2}{2} \quad (A-7)$$

$$h = \sum_i c_i h_i \quad (A-8)$$

$$h_i = \int_0^T c_{p,i} dT + h_i^0 \quad (A-9)$$

In terms of temperature:

$$\begin{aligned} \rho u \bar{c_p} \frac{\partial T}{\partial x} + \rho v \bar{c_p} \frac{\partial T}{\partial y} &= \frac{\partial}{\partial y} \left(k \frac{\partial T}{\partial y} \right) + \mu \frac{\partial u^2}{\partial y} + \sum_i \dot{w}_i (h_i^0 - h_i) \\ &+ \sum_i c_{p,i} D_{12} \frac{\partial c_i}{\partial y} \frac{\partial T}{\partial y} \end{aligned} \quad (A-10)$$

and

$$\bar{c}_p = \sum_i c_i \frac{dh_i}{dT} = \sum_i c_i c_{p,i} \quad . \quad (A-11)$$

in both above equations, on the right-hand side, all gradients with respect to the X direction have been dropped.

d. TRANSFORMATION OF THE BOUNDARY LAYER EQUATIONS

The above mentioned approximate boundary layer equations still constitute a set of nonlinear equations that cannot be solved without further approximations.

In order to transform the nonlinear differential equations to ordinary differential equations, which are separable, the technique suggested by Li and Nagamatsu¹⁵ is used:

$$\psi(x, y) = \frac{1}{p} \int_0^y \rho u dy + \psi(x, 0) \quad (A-12)$$

$$u = \frac{p_\infty}{\rho} \frac{\partial \psi}{\partial y} \quad (A-13)$$

$$v = \frac{p_\infty}{\rho} \frac{\partial \psi}{\partial x}$$

This transformation changes the equations from Cartesian coordinates to stream-function coordinates and the independent variables can now be separated with the help of the substitutions:

$$\begin{aligned} \psi(s, \eta) &= N(s) f(\eta) \\ u(s, \eta) &= U(s) f^1(\eta) \\ c_i(s, \eta) &= c_i(s) z_i(\eta) \\ h_0(s, \eta) &= [h_0(s) g(\eta)] \quad \text{etc.}, \end{aligned} \quad (A-14)$$

where for a flat plate,

$$s = \mu_\infty \rho_\infty u_\infty x \quad (A-15)$$

$$\eta = \frac{1}{2} \sqrt{\frac{\rho_\infty u_\infty}{\mu_\infty x}} \int_0^y \frac{\rho}{\rho_\infty} dy \quad . \quad (A-16)$$

With the assumption of boundary layer similarity, the s dependence of the independent variables disappears, so that the boundary layer properties are not a function of η only.

Here the similarity principle implies that the boundary layer parameter profiles are similar at all x stations, i.e., multiplication by the factor $\sqrt{x/x_{Re}}$ reduces the profiles from all x stations to a single profile at the reference station. For a flat plate and constant, dissociated, free-stream conditions the assumption of a similarity is valid. The new transformation relations are:

$$\begin{aligned}
 \psi &= N_\infty f(\eta) \\
 u &= U_\infty f'(\eta) \\
 c_i &= c_{i\infty} z_i(\eta) \\
 h_0 &= (h_0)_\infty g(\eta)
 \end{aligned} \tag{A-17}$$

The variable η remains the same. The boundary layer equations for a flat plate with uniform external flow finally reduce to:

Equation of Motion:

$$(cf'')' + ff'' = 0 \tag{A-18}$$

Energy:

$$\left(\frac{c}{P_r} g'\right)' + fg = \left[\frac{c}{s} \left(\frac{1}{L} - 1\right) \sum_i \frac{h_i (c_i)_\infty}{(h_0)_\infty} z_i'\right] \tag{A-19}$$

Conservation of Species:

$$\left(\frac{c}{s_a} z_+^t\right)' + fz_+ = \frac{2x\dot{w}_+}{\rho\rho_\infty u_\infty^2 \mu_\infty} \tag{A-20}$$

where

$$C = \frac{\rho\mu}{\rho\mu_\infty} \quad P_r = \frac{\mu c_p}{k} \quad S = \frac{\mu}{\rho D_{12}} \quad S_a = \frac{\mu}{\rho D_a} \quad L = \frac{\rho D_{12} \bar{c}_p}{k}$$

The boundary conditions for a cold, catalytic wall are

$$\begin{array}{ll}
 \text{at } y = 0 & \eta = 0 \\
 z_i(0) = z_{i*} = \frac{c_{+*}}{c_{+\infty}} \sim 0 & \text{at } y = \infty \quad \eta = \infty \\
 f(0) = f_* & f(\infty) \rightarrow 0 \\
 f'(0) = 0 & f'(\infty) \rightarrow 1 \\
 g(0) = g_* & g(\infty) \rightarrow 1 \\
 g'(0) = g_*^1 & g'(\infty) \rightarrow 0
 \end{array}$$

The above set of differential equations, in the general case of variable coefficients, still does not yield a closed-form solution, but numerical integration is possible and relatively simple. The uncoupling of the energy equation and the equation for the conservation of species reduces the computational labor required considerably. Aside from the general assumptions made at the outset, the accuracy of the above boundary layer equations for the present application is probably at least as good as the accuracy with which the various transport coefficients and the rate constants are known.

E. ZERO- ORDER BOUNDARY LAYER APPROXIMATION

If one sets $C = 1$, $P_r = 1$, $L = 1$, $S = S_a = 1$ in the transformed differential boundary layer equations [Eqs. (A-18) through (A-20)] and assumes frozen flow, the equations reduce to

Momentum:

$$f''' + ff'' = 0 \quad (\text{A-21})$$

Specie Concentration:

$$z_+'' + fz' = 0 \quad (\text{A-22})$$

Energy Equation:

$$g'' + fg' = 0 \quad (\text{A-23})$$

The momentum equation is now essentially in the form of the well-known Blasius boundary layer equation for incompressible flow. For the Blasius differential equation, numerical solutions are available in tabulated²¹ form.

From the definitions of $f'(\eta)$, the boundary layer velocity profile is given as:

$$\frac{u}{u_\infty} = f'(\eta) \quad (A-24)$$

and the three boundary conditions are:

$$\begin{aligned} y &= 0 & \eta &= 0 & y &= \infty, & \eta &= \infty \\ f(0) &= 0 & & & & & & \\ f'(0) &= \frac{u}{u_\infty} = 0 & & & f(\infty) &= \frac{u}{u_\infty} = 1 & & . \end{aligned}$$

If one substitutes

$$\begin{aligned} z_+ &= f'(\eta) \\ g &= f'(\eta) \end{aligned} \quad (A-25)$$

into the species conservation and energy equation, one reduces these equations to the Blasius equation. For a cold catalytic wall, $(Z_+)_w = 0$ and

$$z_+ = f(\eta) = \frac{u}{u_\infty} . \quad (A-26)$$

This equation is Probstein's second integral. It indicates that, for the above assumptions, the ion mass fraction in the boundary layer varies similarly as the x component of velocity. By definition,

$$z_+ \equiv \frac{n_{+m_+}/\rho}{[n_{+m_+}/\rho]_\infty} . \quad (A-27)$$

From this relation, the ion density profile in the boundary layer is obtained as:

$$n_{+m_+} = z_+ \frac{\rho}{\rho_\infty} n_{+\infty} = \frac{u}{u_\infty} \frac{\rho}{\rho_\infty} n_{+\infty} . \quad (A-28)$$

A similar expression can be found for the enthalpy profile; however, for this application one is more interested in the temperature profile. If, in addition to the previous assumptions, one neglects the effect of diffusion of atoms on the temperature profile in the boundary layer, the differential equation for the normalized temperature profile may be expressed as:

$$T^{*''} + P_r f T^{*'} = - \frac{P_r}{4} (\gamma_\infty - 1) M_\infty^2 (f'')^2 , \quad (A-29)$$

where

$$T^* = T/T_\infty .$$

This equation for the temperature profile has been solved by Chapman and Rubesin¹⁸ and the solution is given by:

$$\frac{T}{T_\infty} = 1 + \frac{\gamma_\infty - 1}{W} M_\infty^2 r(\eta) + a_0 Y_0(\eta) . \quad (A-30)$$

The functions $r(\eta)$ and $Y_0(\eta)$ are given in Ref. 18 for $P_r = 0.72$. These functions have been recalculated for $P_r = 1$ for the present purpose. The appropriate boundary conditions are:

$$Y_0(0) = 1 \quad Y_0(\infty) = 0$$

$$r(0) = \sqrt{P_r} \quad r(\infty) = 0 .$$

The temperature profiles have been computed using equilibrium free stream γ_∞ and M_∞ values, and correspond to the profiles associated with frozen-flow conditions. The error in estimated probe current due to the approximated temperature profile is probably not larger than a factor of $\sqrt{2}$. The effect of inaccurate temperature profiles will be felt more strongly in the relationship between the boundary layer parameter η and y , and will yield thermal boundary layers thinner than the actual boundary layer.

Near the cold wall, large gradients exist in both the temperature and ion concentration profiles, and relatively small changes of y correspond to large changes in the numerical values of ion concentration.

Following Chapman and Rubesin,¹⁸ the relation between the boundary layer transformation parameter η and the physical distance y from the flat plate surface is given by:

$$\eta = \frac{1}{2} \sqrt{\frac{\rho_\infty u_\infty}{\mu_\infty x C_1}} \int_0^y \frac{\rho}{\rho_\infty} dy \quad . \quad (A-31)$$

now, since

$$\frac{\rho}{\rho_\infty} = \frac{T_\infty}{T} \frac{\bar{m}}{\bar{m}_\infty} \quad , \quad (A-32)$$

$$y \approx 2 \sqrt{\frac{\mu_\infty x C_1}{u_\infty \rho_\infty}} \int_0^\eta \frac{T}{T_\infty} d\eta' \quad , \quad (A-33)$$

assuming that $\bar{m}_\infty/\bar{m} \sim 1$. Substituting for T/T_∞ from the energy equation and integrating, the relation between y and η becomes

$$y = 2 \sqrt{\frac{\mu_\infty x C_1}{\rho_\infty u_\infty}} \left[\eta + \frac{\gamma - 1}{2} M_\infty^2 \bar{r}(\eta) + a_0 \bar{Y}_0(\eta) \right] \quad (A-34)$$

where the functions,

$$(\bar{r} \eta) = \int_0^\eta r(\eta') d\eta' \quad \bar{Y}(\eta) = \int_0^\eta \bar{Y}_0(\eta') d\eta' \quad (A-35)$$

have been calculated for $P_r = 1$. It is evident that an underestimation of local temperature will yield boundary layers that are too thin. This effect is felt most severely near the wall, where the integral is still small. However, underestimation of local temperature will be offset to some extent by the assumption of a constant molecular weight across the boundary layer.

APPENDIX B

PRESSURE-DRIVEN SHOCK TUBE

APPENDIX B

PRESSURE-DRIVEN SHOCK TUBE

The laboratory simulation of plasma phenomena associated with planetary re-entry conditions, such as voltage breakdown during re-entry, and communication "blackout," operation of free-stream and flush-mounted ion probes on re-entry vehicles, etc., necessitate the existence of a high-velocity plasma. In addition, studies of the strong shock ionization precursor effects and investigations of the shock front nonequilibrium radiation overshoot require the production of very-high-velocity shocks. For short test times, the arc-driven shock tube can provide strong shocks and equilibrium plasmas moving with velocities up to about 40,000 ft/sec. One general advantage of shock-tube testing is that, if equilibrium test conditions exist in the test slug, the gas properties are a function only of shock velocity. Thus, an accurate measurement of shock velocity yields all equilibrium gas properties.

1. DESCRIPTION OF THE EQUIPMENT

The shock tube used in these studies is of the arc-driven type and is modeled after the design of Camm and Rose.² A schematic of the shock tube is presented in Fig. B-1. Figure B-2 shows a cross section through the shock tube driver. The driver is 1½-inches in diameter and 12 inches long. The driver is connected to the 12-inch diameter driven tube by means of a 54 inch long circular transition section. The length of the driven tube has recently been increased from 25 to 36 feet.

The energy source is a 100 kilojoule capacitor bank, which is triggered by an exploding wire technique.

2. INSTRUMENTATION

Shock velocity is measured by a series of flush probes mounted in the tube walls. The probe current develops a voltage across a resistor. This voltage is then differentiated to give a spike in voltage when the ionization front passes the probe. The voltage spike is applied to the vertical plates of a raster oscilloscope (see Fig. B-3), and the time for the

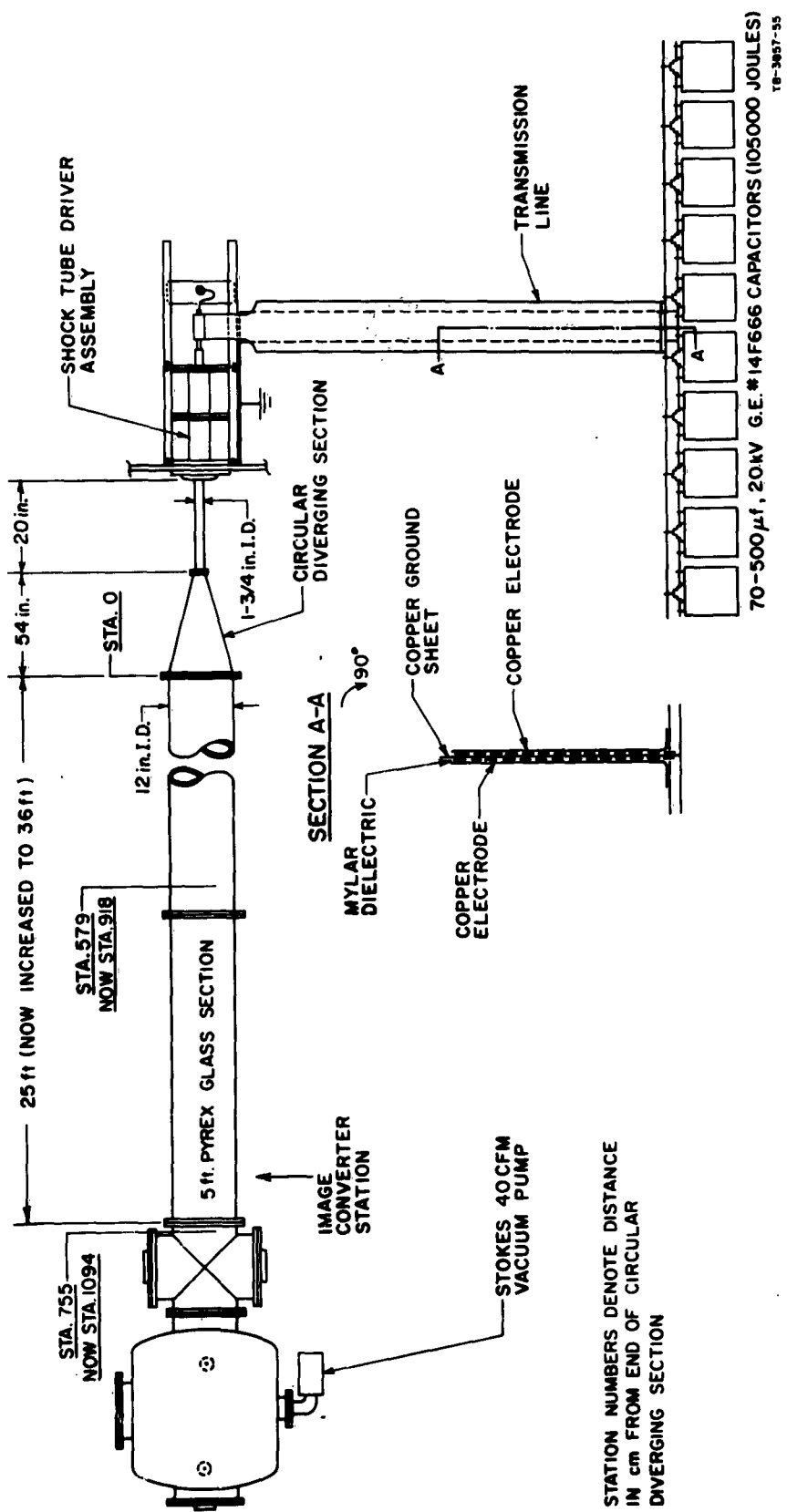


FIG. B-1 SCHEMATIC LAYOUT OF PRESSURE-DRIVEN, ARC-HEATED SHOCK TUBE

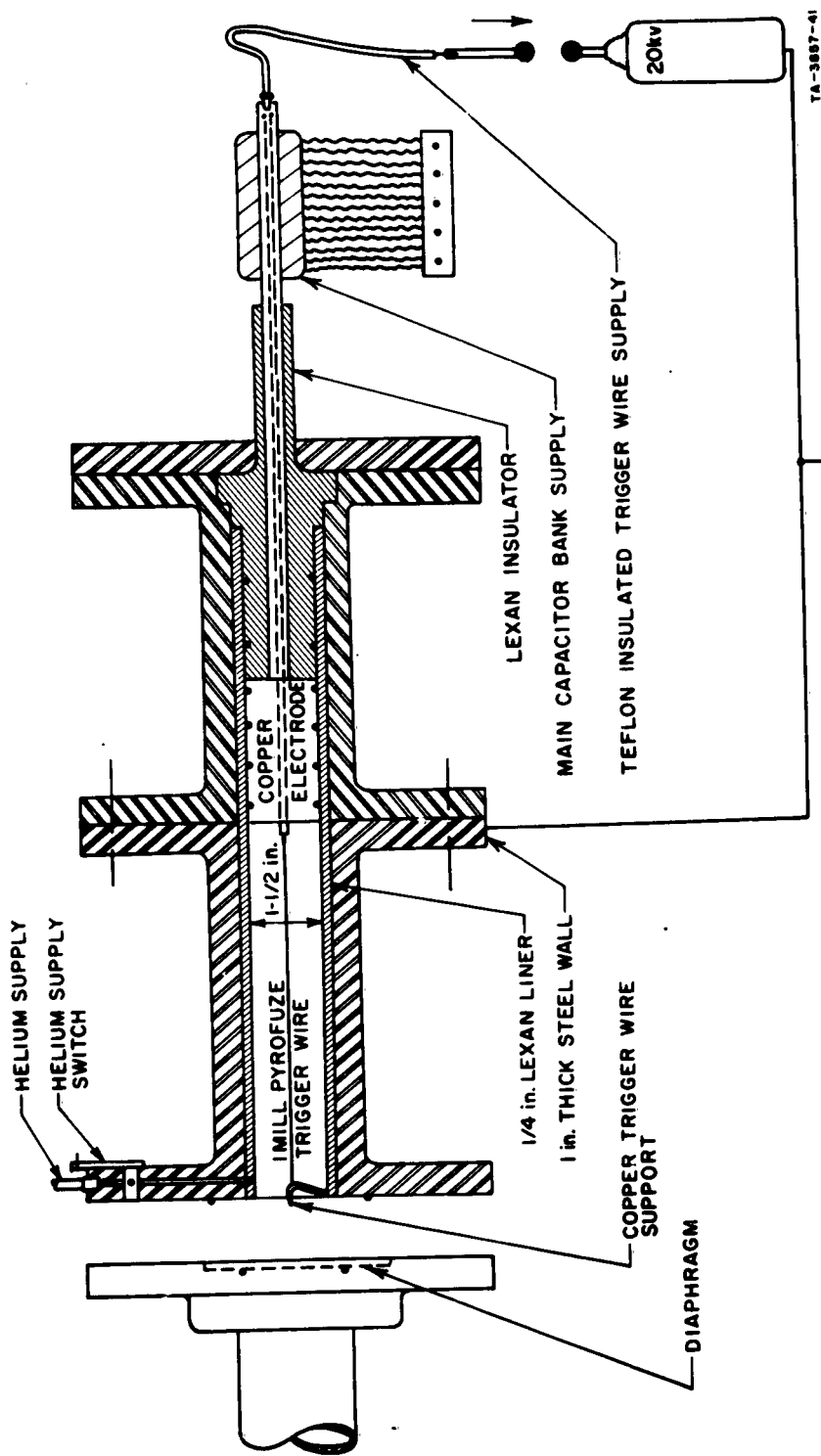


FIG. B-2 CROSS SECTION OF SHOCK TUBE DRIVER

$P_i = 1 \text{ mm}$
 $(U_s)_{\text{AVG}} = 4.5 \text{ mm}/\mu\text{sec}$
 $100 \mu\text{sec}/\text{line}$



TA-3007-44

FIG. B-3 SHOCK VELOCITY MEASUREMENT ON RASTER SCOPE

shock to travel a known distance is measured from the oscilloscope in terms of the time between spikes. The accuracy with which velocity is measured is estimated to be about 2 percent. Typical response curves of various instruments used on the shock tube are shown in Figs. B-3 through B-7.

Figure B-4 shows a pressure probe trace and the time resolved response of a 0.5 mm diameter platinum free-stream ion probe. Note the indicated flat ion density level in the test gas slug and the increased probe response when the interface arrives. (The increased interface

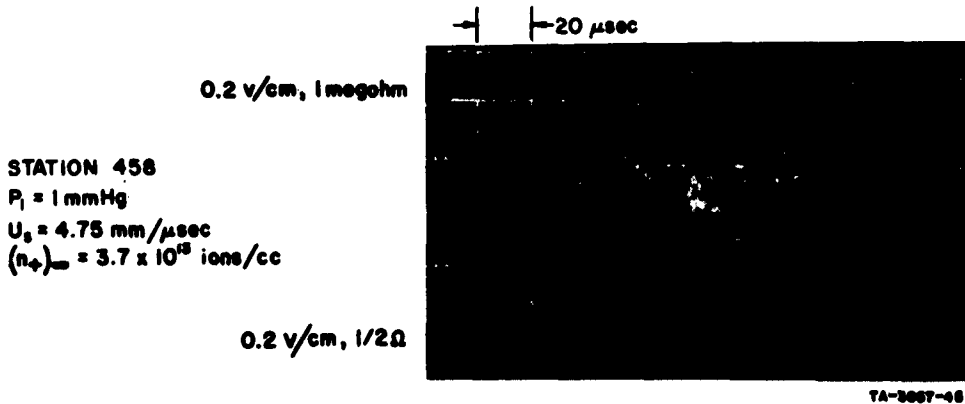


FIG. B-4 COMPARISON OF FLUSH-MOUNTED PRESSURE PROBE RESPONSE AND 0.25×6.3 mm FREE-STREAM ION PROBE RESPONSE
 Upper Trace: Pressure Probe
 Lower Trace: Free-Stream Ion Probe

response is attributed to the arrival of driver impurities having lower ionization potential than air.) It should also be realized that the ion probe measures only the local ion density level, so that, in general, one cannot conclude from these data anything in regard to the state of the gas at other localities in the test slug. On the other hand, this statement can be turned around to say that for experiments involving ion probes, only the local test conditions are important. This fact has been utilized, since experimental experience has indicated that test times in the center of the shock tube can be substantially lower than test times near the shock tube wall.

Figures B-5 and B-6 show typical photomultiplier traces at 1 mmHg and 0.1 mmHg initial shock tube pressure, respectively. In Fig. B-5 note

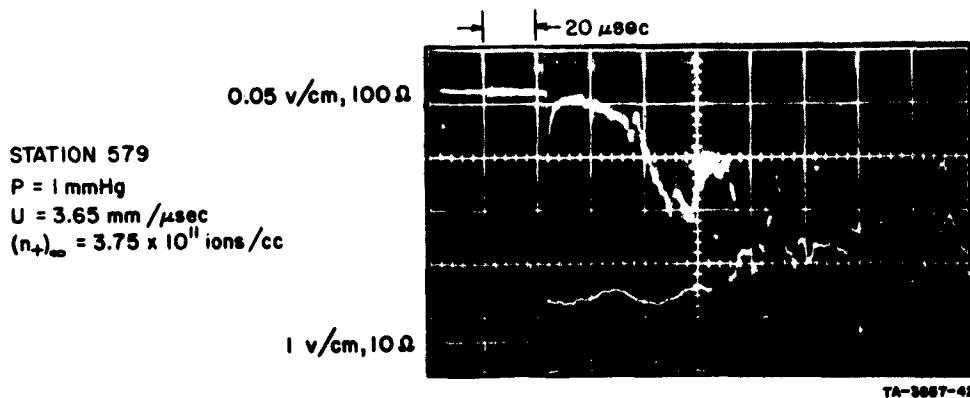


FIG. B-5 TYPICAL PHOTOMULTIPLIER RESPONSE
FOR 1 mmHg INITIAL SHOCK TUBE PRESSURE
Upper Trace: Photomultiplier
Lower Trace: Free-Stream Ion Probe, 0.25 mm dia \times 6.3 mm Long

that the local indicated test time of the ion probe, located outside the photomultiplier field of view, is about twice as long as indicated by the photomultiplier. The test time, as observed at a given shock tube station is defined as the time interval from the arrival of the shock front to the arrival of the interface. It is also interesting to observe that the ion probe response reaches a steady level sooner than the photomultiplier, and then remains constant, despite the fact that chemical relaxation is still proceeding. The photomultiplier field of view is directly along a shock tube diameter. Collimation is achieved by two 0.15 mm wide slots placed 12 inches apart. The aperture slots are about 3.25 mm long.

response is attributed to the arrival of driver impurities having lower ionization potential than air.) It should also be realized that the ion probe measures only the local ion density level, so that, in general, one cannot conclude from these data anything in regard to the state of the gas at other localities in the test slug. On the other hand, this statement can be turned around to say that for experiments involving ion probes, only the local test conditions are important. This fact has been utilized, since experimental experience has indicated that test times in the center of the shock tube can be substantially lower than test times near the shock tube wall.

Figures B-5 and B-6 show typical photomultiplier traces at 1 mmHg and 0.1 mmHg initial shock tube pressure, respectively. In Fig. B-5 note

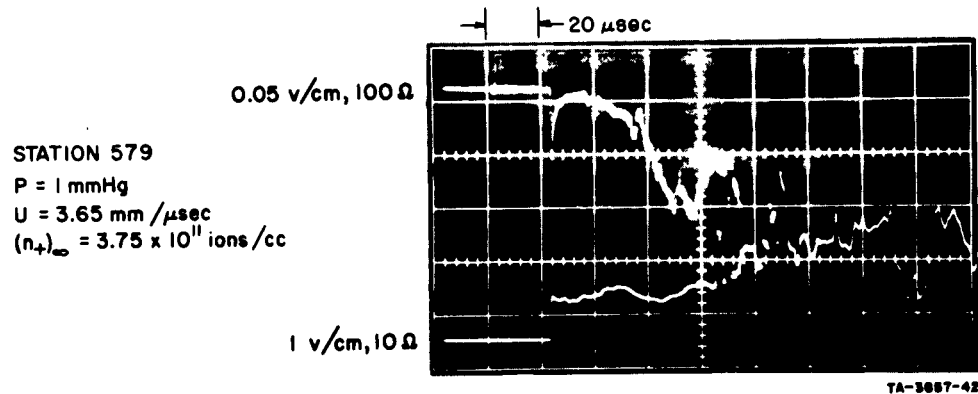


FIG. B-5 TYPICAL PHOTOMULTIPLIER RESPONSE
FOR 1 mmHg INITIAL SHOCK TUBE PRESSURE
Upper Trace: Photomultiplier
Lower Trace: Free-Stream Ion Probe, 0.25 mm dia \times 6.3 mm Long

that the local indicated test time of the ion probe, located outside the photomultiplier field of view, is about twice as long as indicated by the photomultiplier. The test time, as observed at a given shock tube station is defined as the time interval from the arrival of the shock front to the arrival of the interface. It is also interesting to observe that the ion probe response reaches a steady level sooner than the photomultiplier, and then remains constant, despite the fact that chemical relaxation is still proceeding. The photomultiplier field of view is directly along a shock tube diameter. Collimation is achieved by two 0.15 mm wide slots placed 12 inches apart. The aperture slots are about 3.25 mm long.

In contrast to the photomultiplier response corresponding to shock conditions at 1 mmHg initial pressures, the photomultiplier trace at 0.1 mm initial pressure, shown in Fig. B-6, does not indicate any increased radiation interface activity. Consequently, at low pressure, photomultipliers do not give a good indication of test time.

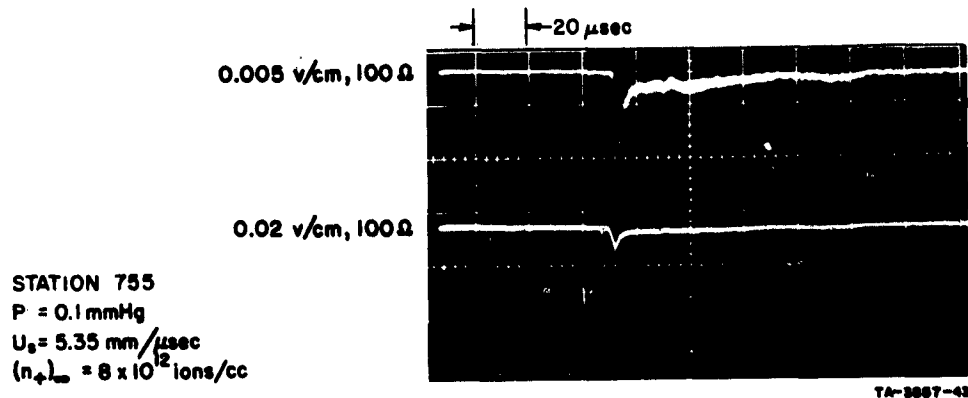


FIG. B-6 TYPICAL PHOTOMULTIPLIER RESPONSE
FOR 0.1 mmHg INITIAL SHOCK TUBE PRESSURE
AND LOW SHOCK VELOCITY AT THAT PRESSURE

Figure B-7 shows some image converter photographs. In the upper picture, taken at 1 mmHg initial shock tube pressure, the shock interface separation at the time was always too large to be recorded on the same shot. The picture indicates the flow field structure about the flat end of a one inch diameter cylinder. In the lower photograph at 0.1 mmHg initial pressure, the ragged interface is vividly apparent, indicating almost no test time. An ion probe sitting in the lower part of the tube would indicate test time of the order of 10 μ sec.

Shock velocity versus capacitor energy input into the driver is shown in Fig. B-8. To date the shock tube has been tested at 1 mmHg and 0.1 mmHg initial pressures. The capacitor bank voltage variation ranged from 7 kv to 15 kv. It is perhaps worth mentioning that our particular driver triggering system has permitted us to break down the driver gas at very low voltages, say 6.5 kv, and 200 psi driver pressures without difficulties.

Figures B-9 and B-10 present the observed shock tube test times about 19 ft from the exit of the diverging section for 1 mmHg and 0.1 mmHg

FLOW ABOUT 1 INCH DIAMETER CYLINDER,
FLAT END OF CYLINDER IS FACING FLOW.
SHOCK FRONT NOT VERY BRIGHT, BECAUSE
U.V. RADIATION IS ABSORBED IN PYREX
GLASS. BRIGHT LINE BEHIND SHOCK
FRONT IS 1/4 - INCH BRASS SUPPORT ROD

STATION 719

$P_t = 1 \text{ mmHg}$

$U_s = 4.5 \text{ mm}/\mu\text{sec}$



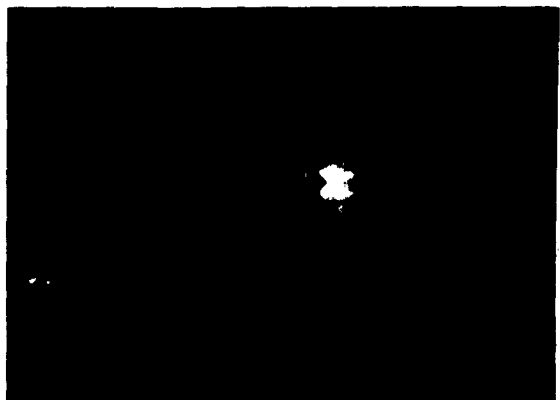
NOTE RUGGED INTERFACE: LOCAL TEST
TIME VARIES FROM A $2\mu\text{sec}$ MINIMUM TO
ABOUT $8\mu\text{sec}$ MAXIMUM

STATION 719

$P_t = 0.1 \text{ mmHg}$

$U_s = 6.5 \text{ mm}/\mu\text{sec}$

SHOCK FRONT HAS BEEN ENHANCED



TA-3007-46

FIG. B-7 IMAGE CONVERTER PICTURES
(Courtesy, Electro Optical Corp.)

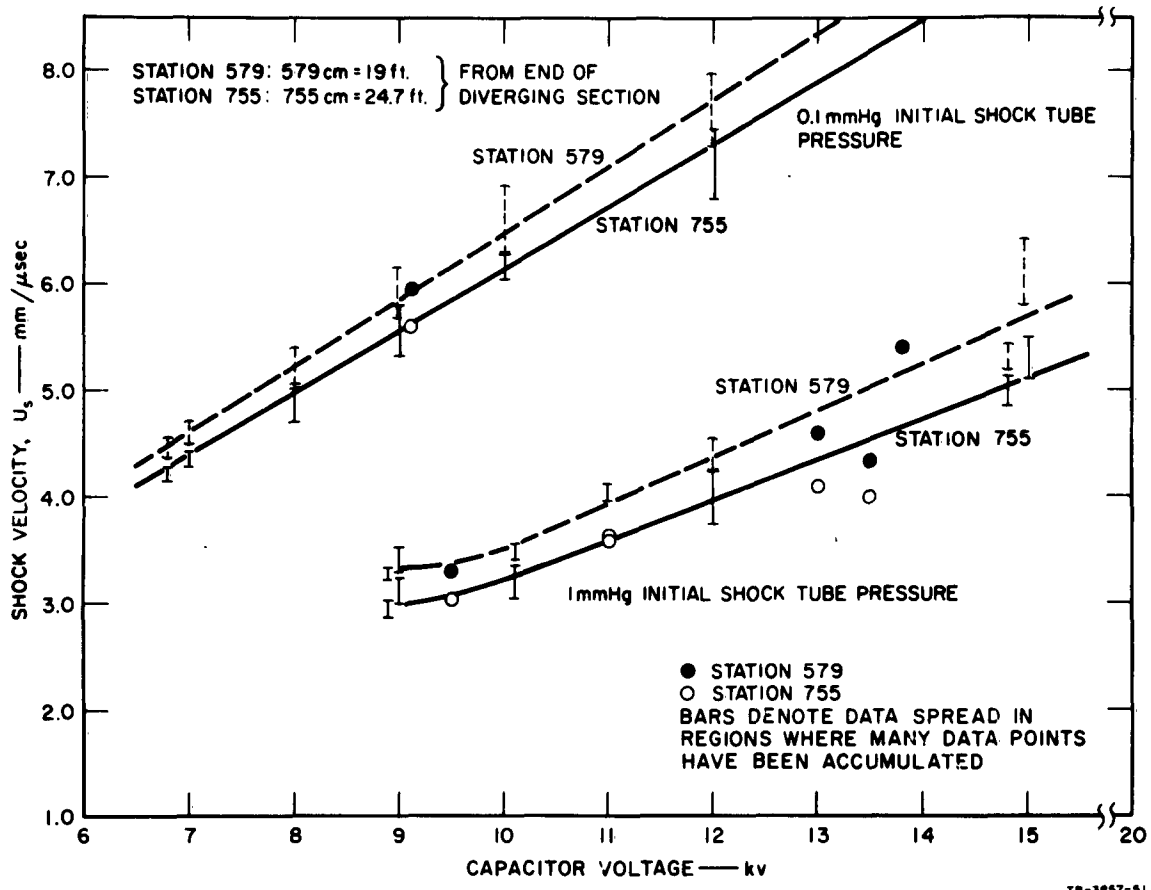


FIG. B-8 SHOCK VELOCITY vs. CAPACITOR VOLTAGE
 FOR PRESSURE-DRIVEN, ARC-HEATED SHOCK TUBE

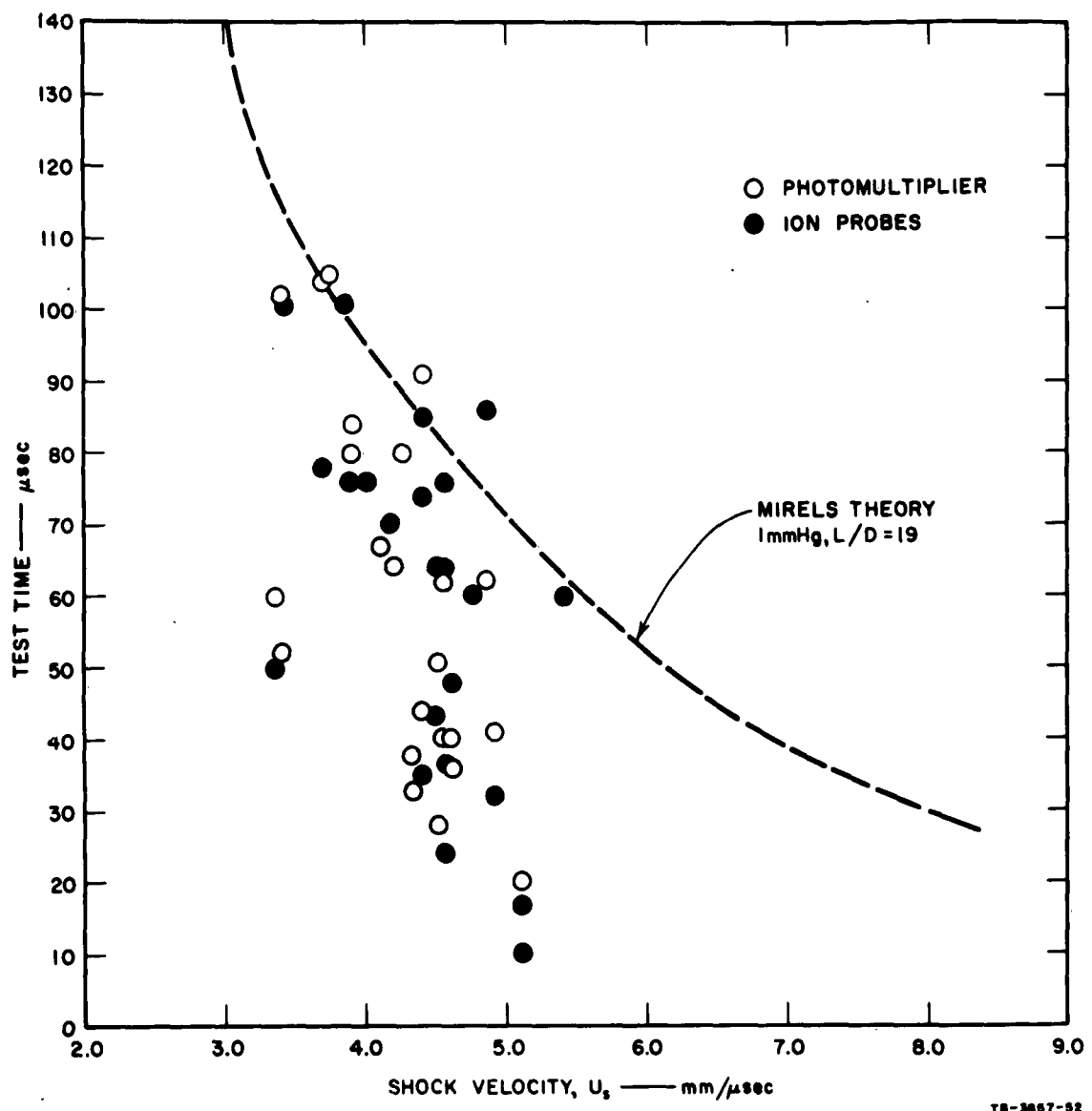


FIG. B-9 SHOCK TUBE TEST TIMES vs. SHOCK VELOCITY
AT 1 mmHg INITIAL SHOCK TUBE PRESSURE

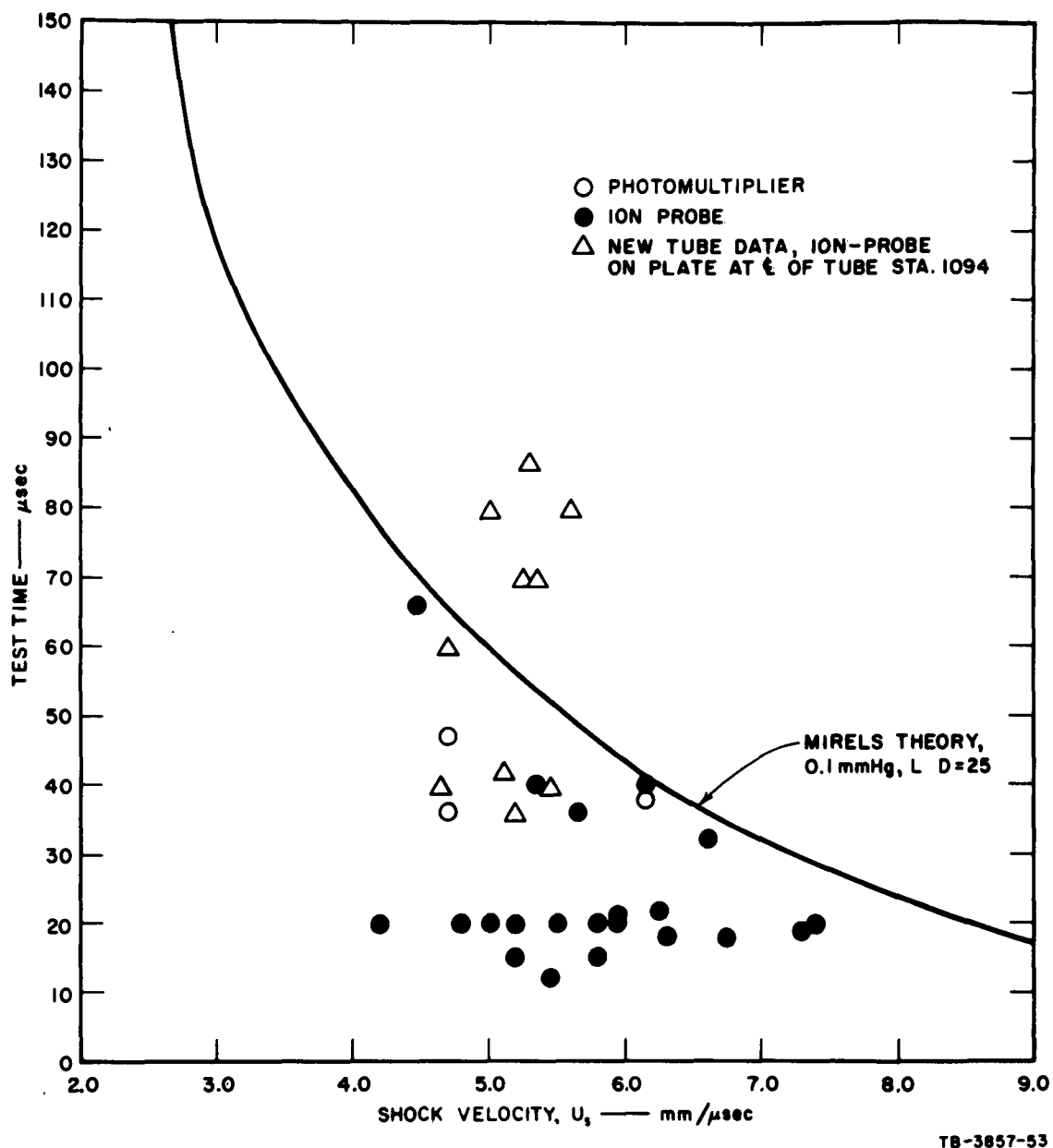


FIG. B-10 SHOCK TUBE TEST TIMES vs. SHOCK VELOCITY
AT 0.1 mmHg INITIAL SHOCK TUBE PRESSURE

initial shock tube pressures, respectively. The test times were obtained from observations of photomultiplier response characteristics and from ion probes. Photomultiplier test times correspond to the time between the center of the initial spiked deflection and the secondary increase in radiation level, generally associated with the interface. Test times obtained from ion probes were similarly counted from the initial rise due to the shock front to the subsequent increase in activity when the interface arrives. At low shock velocities, however, no significant increase in instrument deflection is observed by either the photomultiplier or the ion probes. In those cases, an arbitrary minimum fluctuation level of about 50 percent is set; when probe current fluctuations exceed this level, the interface is presumed to have arrived.

Theoretical test time expectations, using Mirel's²³ equations, have been superimposed on the experimental results in Figs. B-9 and B-10 for an L/D ratio of 19. The wide scatter of experimental data points is characteristic of arc-driven shock tubes (see for example, reports from Avco²² and JPL²⁴). Note that a few data points fall above the theoretical curve; this is probably due to the fact that we based our L/D ratio on the distance from the diverging channel exit rather than on the distance from the diaphragm. The diaphragm is about 5 ft upstream of the diverging channel exit, but over this distance the channel tube cross section varies from a $1\frac{1}{2}$ inch diameter to the 12 inch test tube diameter.

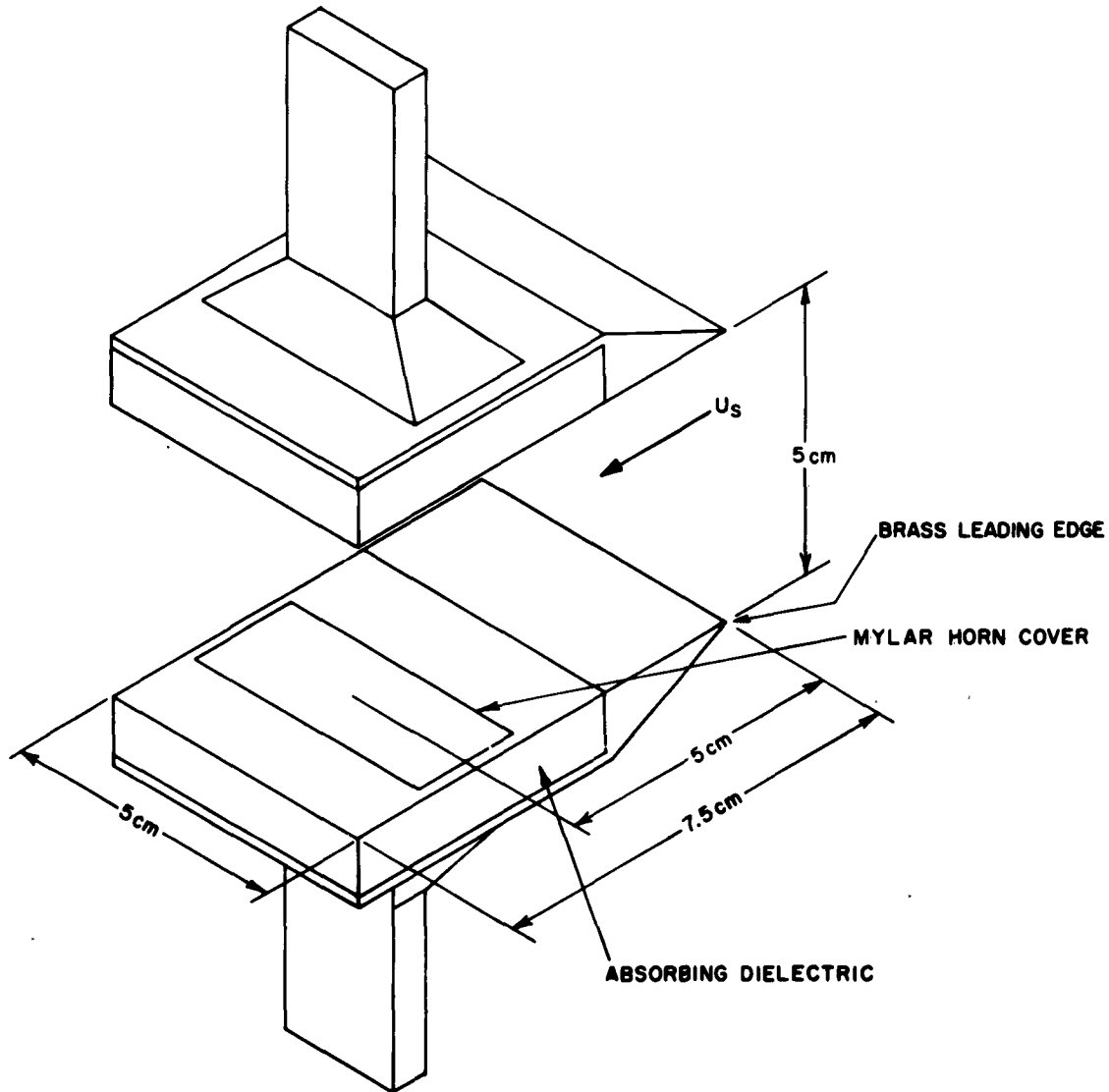
Since the original shock tube length was short, $L/D \leq 25$, even the calculated theoretical test times are short. To remedy the situation, the L/D was recently increased to 36. A few test times observed at the new far end position are also plotted on the graph. Often, the photomultipliers indicated substantially shorter test times than did the free-stream ion probes placed about 1 to 2 inches into the shock tube. This indicated a curved interface with the flow in the center of the tube projecting forward by about 3 to 10 inches relative to the flow near the wall. The existence of a curved interface was visually verified from the image converter (see Fig. B-7).

3. TEST FOR EQUILIBRIUM

Measurements were made at 0.1 and 1.0 mmHg to check that the slug of ionized gas was indeed in ionization equilibrium. This was done by phase measurements made at 33 Gc with a microwave interferometer. The transmission path was between a pair of horns spaced 2 inches apart and

located symmetrically about the tube axis (see Fig. B-11). The horns were mounted so that their apertures were flush with the surface of the plates, 2 inches from the plate leading edge. The plates were 2 inches wide and 3 inches long with sharp tapers at their leading edges to minimize flow disturbances. The horn apertures were covered with Mylar tape.

Using this system, electron densities were checked over the range of 10^{10} to 3×10^{12} elec/cc at 1 mmHg. Typical instrument responses are



TA-3687-48

FIG. B-11 EXPERIMENTAL CONFIGURATION OF MICROWAVE INTERFEROMETER

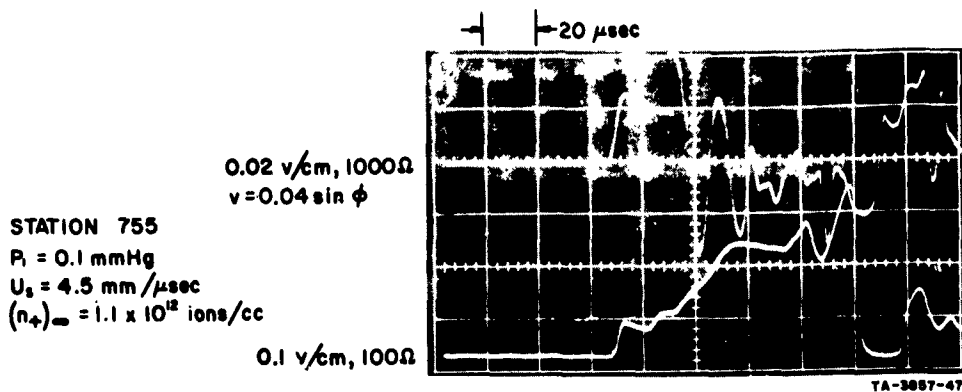


FIG. B-12 EQUILIBRIUM SLUG ELECTRON DENSITY MEASURED WITH MICROWAVE INTERFEROMETER AT 0.1 mmHg INITIAL SHOCK TUBE PRESSURE AND RESPONSE OF 0.25 mm dia FREE-STREAM ION PROBE
 (Upper Trace: Interferometer)
 (Lower Trace: Ion Probe)

presented in Figs. B-12 and B-13. The electron densities inferred from the interferometer measurements agreed to within 30 percent of the values of the equilibrium electron densities calculated from the measured data on shock velocity. These results were obtained with the tube fired over thirty times without cleaning.

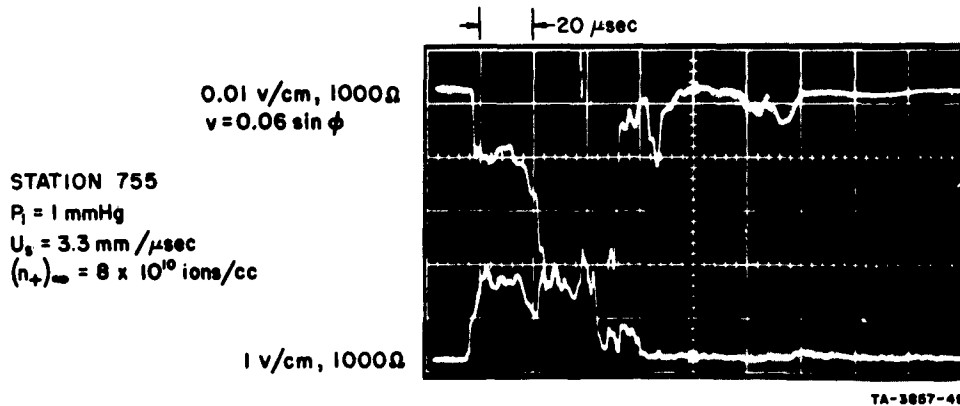


FIG. B-13 EQUILIBRIUM SLUG ELECTRON DENSITY MEASURED WITH MICROWAVE INTERFEROMETER AT 1 mmHg INITIAL SHOCK TUBE PRESSURE AND RESPONSE OF 0.25 mm dia FREE-STREAM ION PROBE
 (Upper Trace: Interferometer)
 (Lower Trace: Free-Stream Ion Probe)

The tube was also operated with dry air as well as ordinary room air. No significant difference was detectable either with probes, or with the interferometer. Neither was a change in agreement with equilibrium calculations detected.

Measurements made at 0.1 mmHg showed more sensitivity to tube cleanliness when fired at slower velocities. Measurements made with 40 shots on the tube without cleaning indicated electron densities as much as an order of magnitude *lower* than equilibrium. After cleaning, the interferometer still read lower electron densities than equilibrium, but the level was raised to within a factor of two of equilibrium. A 0.25×6.4 mm probe mounted between the interferometer plates indicated electron densities close to those deduced from the interferometer. A similar probe mounted forward of the interferometer plates indicated electron densities higher than the probe mounted between the plates. The forward probe measured values closer to equilibrium than the probe mounted between the plates.

These results indicate that the plates were disturbing the flow at 0.1 mmHg initial pressures and causing a lower electron density to appear between the plates than exists in free stream. The free-stream electron density as measured by the forward probe indicated electron densities within a factor of two of equilibrium. The agreement between the interferometer and the probe located between the plates is taken as evidence that the 0.25 mm free-stream probe is accurately measuring the electron density.

Measurements made with identical probe space 120 degrees apart around the circumference of the tube indicate that variations in electron density around the tube can be as high as a factor of two.

APPENDIX C

TEST FACILITIES USED IN THE RVIP EXPERIMENTAL PROGRAM

APPENDIX C

TEST FACILITIES USED IN THE RVIP EXPERIMENTAL PROGRAM

1. ELECTROMAGNETIC SHOCK TUBE

The electromagnetic shock tube used in this investigation is shown in Figs. C-1 and C-2. The discharge section consists of a tapered glass tube with a solid electrode at the small end and a ring electrode at the large end where the cylindrical pipe begins. The shock tube proper is a 15 cm-ID Pyrex pipe as shown in Fig. C-2. The $30 \mu\text{fd}$, 20-kv capacitors, the charging power supply, and appropriate switch gear are housed within a metal enclosure (inset). The enclosure also houses the discharge section as indicated in the inset of Fig. C-2. The heavy top plate to which the pump ring and cylindrical test section are attached also serves as the ring electrode of the discharge section. The switch between the capacitors and the central electrode is activated by reducing the pressure in the switch section [Fig. C-1] until breakdown occurs. The shock tube is capable of producing plasma flows greater than $1 \text{ cm}/\mu\text{sec}$ and electron densities greater than 10^{14} electrons/cc. A description of the shock tube performance, including an evaluation of Langmuir probe performance in this environment, can be found elsewhere.^{25,26}

For these measurements, the tube was evacuated to 0.1 mmHg and fired at 9 kv. Under these conditions, the shock velocity is less than $2.0 \text{ mm}/\mu\text{sec}$ and the electron temperature behind the shock is estimated (from swept Langmuir probe measurements) to be 5000°K . Under these conditions, the ion drift velocity (approximately equal to the shock velocity) is less than the thermal velocity of the ions (approximately 3.5 mm/sec). Some of the measurements were performed in the region milliseconds after the shock front passed so that the ion drift velocity approached zero and the electron temperature became 300°K (inferred from swept Langmuir probes).

2. LOW-PRESSURE FLAME FACILITY

The low-pressure chamber is a 20-inch cylindrical section of Pyrex glass. Two 4-inch diameter ports have been added on opposite sides to

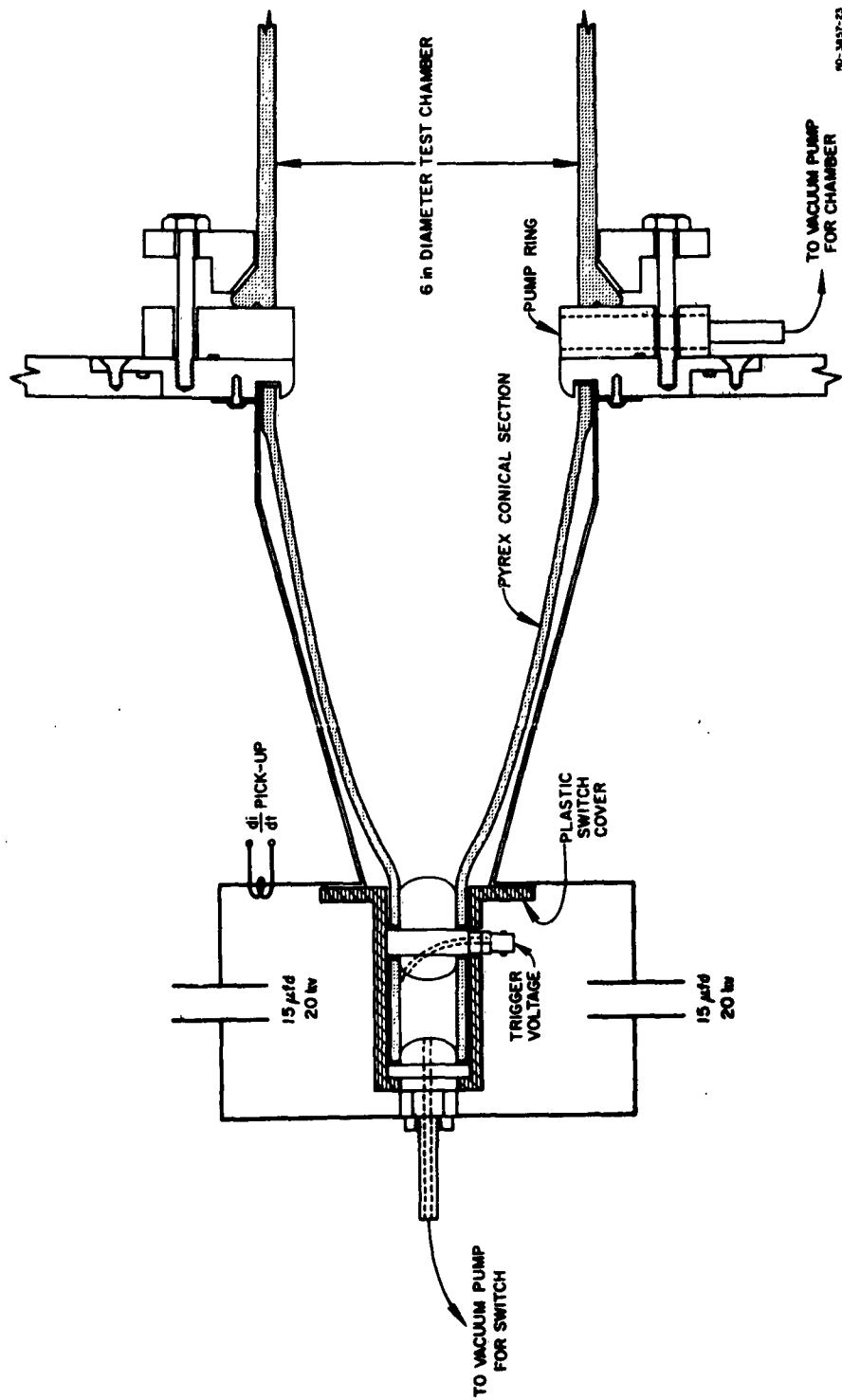


FIG. C-1 DETAIL OF CONICAL DISCHARGE SECTION OF THE ELECTROMAGNETIC SHOCK TUBE



FIG. C-2 PHOTOGRAPH OF ELECTROMAGNETIC SHOCK TUBE

provide flat glass viewing areas. All access to the chamber is through the base plate. The steel plate forming the top of the chamber has a short section of the 4-inch exhaust line above it, a water-cooled baffle section to further cool the gas and a mixed ethylene-oxygen flame is used in this measurement. Figure 2 shows the test facility, including the visible flame. A description of the facility is in Ref. 23.

For these measurements, the flame was burned at 7 mm diameter with potassium or sodium chloride. The flame temperature was determined by a sodium line reversal measurement. Microscopic static probe measurements of the charged particle density show that the charged particle density is in Saha equilibrium with the density and temperature. These measurements further indicate the absence of a negligible number of negative ions.



FIG. C-3 ETHYLENE-OXYGEN FLAME BURNING AT 8 mmHg PRESSURE

REFERENCES

1. I. Langmuir and H. Mott-Smith, "Studies of Electric Discharges at Low Pressures," *General Electric Review* 27, Nos. 7, 8, 9, pp. 449-455, 538-548, 616-623 (July, August, September 1924).
2. D. Bohm, E. H. S. Burhop, and H. S. W. Massey, "The Use of Probes for Plasma Exploration in Strong Magnetic Fields," in *Characteristics of Electrical Discharges in Magnetic Fields*, pp. 13-76, Ed. Guthrie and Wakerling, (McGraw-Hill Book Company, New York, N.Y., 1949).
3. G. Schultz and S. C. Brown, "Microwave Study of Positive Ion Collection by Probes," *Phys. Rev.* 98, No. 6, pp. 1642-1649 (15 June 1955).
4. G. Hok, et al., "Dynamic Probe Measurements in the Ionosphere," *Scientific Report FS-3*, University of Michigan Research Institute, Reprinted under Contract AF 19(604)-1843 (November 1958).
5. J. F. Allen, R. L. F. Boyd, and P. Reynolds, "The Collection of Positive Ions by a Probe Immersed in a Plasma," *Proc. Phys. Soc. (London) Sec. B* 5, p. 70 (1957).
6. E. O. Johnson and L. Malter, "A Floating Double Method for Measurements in Gas Discharge," *Phys. Rev.* 80, No. 1, pp. 56-68 (1 October 1950).
7. W. E. Scharfman, "The Use of Langmuir Probes to Determine the Electron Density Surrounding Re-Entry Vehicles," Final Report, Contract NAS1-2967, SRI Project 4456, Stanford Research Institute, Menlo Park, California (January 1964).
8. W. R. Hoegy and L. H. Brace, "The Dumbbell Electrostatic Ionosphere Probe: Theoretical Aspects," *Scientific Report JS-1, ORA Projects 2816-1, 03484, and 03599*, Space Physics Research Laboratory, University of Michigan, Ann Arbor, Michigan (September 1961).
9. F. O. Smetana, "On the Current Collected by a Charged Circular Cylinder Immersed in a Two-Dimensional Rarified Plasma Stream," *Proc. Third Symposium on Rarified Gas Dynamics*, Vol. II, pp. 65-91, (Academic Press, New York, N.Y., 1963).
10. J. D. Cobine, *Gaseous Conductors*, pp. 128-129 (Dover Publications, New York, N.Y., 1958).
11. L. Talbot, "Theory of the Stagnation Point Langmuir Probe," *Phys. Fluids* 3, No. 2, pp. 289-297 (March-April 1960).
12. I. Pollin, "The Stagnation-Point Langmuir Probe in a Shock Tube—Theory and Measurements," Report IR-1103, Harry Diamond Laboratories, Army Materiel Command, Washington, D. C. (June 1963).
13. W. H. Dorrance, *Viscous Hypersonic Flow*, (McGraw-Hill Book Company, New York, N.Y., 1962).
14. S. Zivanovic, "Investigation of Precursor Ionization in Front of the Shock Waves of Hypersonic Projectiles," Tech. Report TR 63-217E, Contract DA 04-495-ORD-3567(Z), ARPA Order 347-63, General Motors Defense Research Laboratories, Santa Barbara, California (September 1963).
15. H. D. Weyman, "Electron Diffusion Ahead of Shock Waves in Argon," *Phys. Fluids* 3, No. 4, pp. 545-548 (July-August 1960).
16. D. L. Jones, "Precursor Electrons Ahead of Cylindrical Shock Waves in Argon," *Phys. Fluids* 5, No. 9, pp. 1121-1122 (September 1962).
17. J. C. Camm, et al., "Absolute Intensity of Non-Equilibrium Radiation in Air and Stagnation Point Heating at High Altitudes," *J. Quantitative Spectroscopy and Radiative Transfer* 1, No. 1, pp. 53-75 (September 1961).
18. D. R. Chapman and M. W. Rubesin, "Temperature and Velocity Profiles in the Compressible Laminar Boundary Layer with Arbitrary Distribution of Surface Temperature," *J. Aeron. Sci.* 16, No. 9, pp. 547-565 (September 1949).
19. J. A. Fay and F. R. Riddell, "Theory of Stagnation Point Heat Transfer in Dissociated Air," *Phys. Fluids* 25, No. 2, pp. 73-121 (February 1958).

20. W. D. Hayes and R. F. Probstein, *Hypersonic Flow Theory*, (Academic Press, New York, N.Y., 1959).
21. H. Schlichting, *Boundary Layer Theory*, 7th ~~math~~ Edition (McGraw-Hill Book Company, New York, N.Y., 1960).
22. J. C. Camm and P. H. Rose, "Electric Arc-Driven Shock Tube," *Phys. Fluids* 6, No. 5, pp. 663-678 (May 1963).
23. H. Mirels, "Test Time in Low Pressure Shock Tubes," *Phys. Fluids* 6, No. 9, pp. 1201-1214 (September 1963).
24. D. J. Collins, *et al.*, "Hypervelocity Shock Tube," TR 32-620, Jet Propulsion Laboratory, Pasadena, California (June 1964).
25. W. C. Taylor, "The Use of Ion Probes for Diagnosing Re-Entry Plasmas," Tech Report 11, Contract SD-103, ARPA Order 281-62, SH Project 3857, Stanford Research Institute, Menlo Park, California (July 1963).
26. H. Guthart and T. Morita, "The Magnetic and Ionic Structure of an Electromagnetically Produced Shock," paper accepted for publication in *J. Appl. Phys.*; to appear August 1965.
27. J. Crawford and D. Landauer, "VIP Experiment Subsystem Definition," Program Plan, Issue 2, Contract AF 04(694)-268, General Electric Company (7 February 1964).

DISTRIBUTION LIST

ORGANIZATION	NO. OF COPIES	ORGANIZATION	NO. OF COPIES
Director Advanced Research Projects Agency ATTN: Maj. J. Kiernan ATTN: Dr. Bruce S. Fisher ATTN: F. A. Koether ATTN: C. E. McLain Washington, D. C., 20301	1	Avco-Everett Research Laboratory ATTN: Technical Library, ATTN: Dr. Bennett Kivel 2385 Revere Beach Parkway Everett 49, Massachusetts	2
Aerojet-General Corporation ATTN: Technical Library P. O. Box 296 Azusa, California	1	Avco Research and Development Division ATTN: H. Bell ATTN: Dr. Harold DeBolt 201 Lowell Street Wilmington, Massachusetts	1
Aeronutronic ATTN: L. H. Linder, Manager Technical Information Services Ford Road Newport Beach, California	1	Commanding Officer Ballistics Research Laboratories ATTN: Dr. B. J. Karpov ATTN: Dr. C. H. Murphy Aberdeen Proving Ground, Maryland	1
Aerospace Corporation ATTN: Manager of Penetration Aids 2400 E. El Segundo Blvd. El Segundo, California	1	Barnes Engineering Company ATTN: H. W. Yates 30 Commerce Road Stamford, Connecticut	1
Air Force Cambridge Research Laboratories Scientific Library CRREL, Stop 29 L. G. Hanscom Field Bedford, Massachusetts	1	Battelle Memorial Institute ATTN: Battelle-DEFENDER 505 King Avenue Columbus 1, Ohio	1
HQ BSD (AFSC) AF Unit Post Office ATTN: BSRVD Los Angeles 45, California	1	Bell Telephone Laboratories ATTN: C. W. Hoover ATTN: N. H. Brown ATTN: John McCarthy Whippany, New Jersey	1
Commander U.S. Army Missile Command ATTN: AMCPM-ZER-R ATTN: AMSMI-RB ATTN: AMSMI-RRX Redstone Arsenal Alabama, 35809	1	Bendix Systems Division Flight Sciences Department Ann Arbor, Michigan	1
Air Force Ballistic Systems Division ATTN: Maj. T. Deloney, BSYST Norton Air Force Base, California 92409	1	†British Joint Mission British Embassy ATTN: Dr. A. Neville Mosses, Defense Research 3100 Massachusetts Avenue, N. W. Washington, D. C.	1
Commanding Officer U.S. Army Signal Missile Support Agency ATTN: SIGWS-MM-1 ATTN: MEW White Sands Missile Range, New Mexico	1	Brown Engineering Company, Inc. ATTN: Technical Library Huntsville, Alabama	1
U. S. Army Tech. Intel. Agency ATTN: ORDLI Arlington Hall Station Arlington 12, Virginia	1	Canadian Armament Research and Devel. Estab. ATTN: U. S. Army Liaison Officer P. O. Box 1427 Quebec, P. Q., Canada	1
†Australian Embassy ATTN: D. Barnsley, Defense R&D Rep. 2001 Connecticut Avenue, N. W. Washington, D. C.	1	Central Intelligence Agency ATTN: OCR Standard Distribution 2430 E. Street N. W. Washington 25, D. C.	1
Chief of Naval Operations ATTN: OP-07T10 Washington 25, D. C.	1		

DISTRIBUTION LIST

ORGANIZATION	NO. OF COPIES	ORGANIZATION	NO. OF COPIES
Cornell Aeronautical Laboratory, Inc. ATTN: Applied Physics Department ATTN: Dr. W. Wurster P. O. Box 235 Buffalo 21, New York	1	Lincoln Laboratory ATTN: Dr. S. Edelberg ATTN: Dr. M. Herlin 244 Wood Street Lexington, Massachusetts 02173	1
Defense Documentation Center Cameron Station Alexandria, Virginia	20	Commander U. S. Naval Laboratory ATTN: Librarian White Oak, Silver Spring, Maryland	1
Electro-Optical Systems, Inc. ATTN: Mr. Denison 300 N. Halstead Street Pasadena, California	1	Director U. S. Naval Research Laboratory ATTN: Code 2027 Washington 25, D. C.	1
General Applied Science Laboratories Merrick and Stewart Avenues Westbury, Long Island, New York	1	*Office of Naval Research Department of the Navy ATTN: Dr. S. Silverman, Science Director ATTN: Dr. F. Isakson, Physics Branch ATTN: Mr. M. Cooper, Fluid Dynamics Branch Washington 25, D. C.	1
General Dynamics Corporation/Astronautics ATTN: Mr. K. G. Blair, Chief Librarian Mail Zone 6-157 San Diego Division San Diego 12, California	1	Radio Corporation of America Missile and Surface Radar Division Moorestown, New Jersey	1
General Electric Company, MSVD Document Library Re-Entry Physics Library Unit ATTN: Manager-MSVD Library, Room 3446 3198 Chestnut Street Philadelphia 1, Pa.	1	The RAND Corporation ATTN: Library ATTN: Dr. J. Gross 1700 Main Street Santa Monica, California	1
General Electric Space Science Laboratory ATTN: J. Farber Valley Forge, Pa.	1	Research Laboratory of Electronics Massachusetts Institute of Technology ATTN: George Graham Harvey Cambridge 39, Massachusetts	1
General Motors Defense Research Laboratories ATTN: C. M. Shaar Box T Santa Barbara, California	1	Research Laboratories General Motors Corporation ATTN: Dr. Nils L. Muench Warren, Michigan	2
GCA Corporation ATTN: Library, Technology Division Burlington Road Bedford, Massachusetts, 01730	1	Scientific and Technical Information Facility ATTN: NASA Rep. (SAK/DL) P. O. Box 5700 Bethesda, Maryland 20014	2
Heliodyne Corporation 2365 Westwood Blvd. Los Angeles, 64, California	1	Space Intelligence Division Headquarters, North American Air Defense Command Ent Air Force Base Colorado Springs, Colorado	1
Institute for Defense Analyses ATTN: Dr. J. Menkes ATTN: Dr. L. Biberman ATTN: Dr. R. Fox ATTN: Mr. D. Katcher, JASON Library ATTN: Dr. Hans Wolfhard 400 Army-Navy Drive Arlington, Virginia 22202	1 1 1 1 1	Space Technology Laboratories ATTN: Dr. L. Hromas 1 Space Park Redondo Beach, California	1
Institute of Science and Technology The University of Michigan ATTN: BAMIRAC Library P. O. Box 618 Ann Arbor, Michigan	1	Special Projects Office ATTN: Cdr. Julian, SP-25 Bureau of Weapons Munitions Building Washington 25, D. C.	1
Jet Propulsion Laboratory ATTN: Library 4800 Oak Grove Drive Pasadena, California	1	Stanford Research Institute Communication and Propagation Laboratory ATTN: Mr. Ray L. Leadabrand, Head Propagation Group ATTN: Dr. Carson Flammer Menlo Park, California	1

DISTRIBUTION LIST

ORGANIZATION	NO. OF COPIES	ORGANIZATION	NO. OF COPIES
Sylvania Electronic Systems Applied Research Laboratory ATTN: R. V. Row 100 First Avenue Waltham, Massachusetts	1	Monsanto Research Corporation Boston Laboratory ATTN: Dr. Lucius Gilman Everett, Massachusetts 02149	1
The Warner and Swasey Company Control Instrument Division 32-16 Downing Street Flushing 54, New York	1	†RCA Victor Corporation, Ltd. ATTN: Dr. A. Carswell 1001 Lenoir Street Montreal, Quebec, Canada	1
Dr. Nathan Marcuvitz Polytechnic Institute of Brooklyn 333 Jay Street Brooklyn, New York	1	†Canadian Defense Research Staff ATTN: Mr. Vernon Smith 2450 Massachusetts Avenue, N. W. Washington, D. C.	1
United Aircraft Corporation Research Laboratories ATTN: Dr. Russell G. Meyerand East Hartford, Connecticut	1	MIT-Lincoln Laboratory Press Field Station APO 555, Box 58 San Francisco, California 96555 ATTN: Mr. V. Guethlen	1

* Semi-Annual reports only.

† Research on hypervelocity ranges and air and contaminant chemistry only. Do not include analytical reports on U. S. Missile data or classified reports.

STANFORD
RESEARCH
INSTITUTE

MENLO PARK
CALIFORNIA

Regional Offices and Laboratories

Southern California Laboratories
820 Mission Street
South Pasadena, California 91031

Washington Office
808-17th Street, N.W.
Washington, D.C. 20006

New York Office
270 Park Avenue, Room 1770
New York, New York 10017

Detroit Office
1025 East Maple Road
Birmingham, Michigan 48011

European Office
Pelikanstrasse 37
Zurich 1, Switzerland

Japan Office
Nomura Security Building, 6th Floor
1-1 Nihonbashidori, Chuo-ku
Tokyo, Japan

Retained Representatives

Toronto, Ontario, Canada
Cyril A. Ing
67 Yonge Street, Room 710
Toronto 1, Ontario, Canada

Milan, Italy
Lorenzo Franceschini
Via Macedonio Melloni, 49
Milan, Italy